

A Unified Analytic Framework for Microlensing Caustics: Geode Solutions and Hyper–Catalan Signatures

GLEB BERLOFF  ^{1,*} AND NATALIA G. BERLOFF  ^{2,†}

¹*Department of Physics and Astronomy, University of Warwick, UK*

²*Department of Applied Mathematics and Theoretical Physics, University of Cambridge, UK*

ABSTRACT

We give a preparation-invariant analytic description of image formation near microlensing caustics. After a local Weierstrass preparation at any multiple image (order $d \geq 2$), the lens mapping reduces to a single geode variable m satisfying $m = U \varphi(m)$, where U is a prepared source coordinate and φ is an image-side kernel. The coefficients of $m(U)$ obey closed Hyper–Catalan (HC) recurrences, allowing termwise derivatives and truncation control from the characteristic system. We also use the same form for a short HC predictor–corrector: evaluate the series within its certified radius and apply a brief Newton polish near the boundary. We define an HC signature (first nonzero kernel coefficients) and an HC spectrum (branch points and analyticity radius ρ_U), which quantify sparsity, stiffness, and safe evaluation domains. The construction covers folds and cusps of any global degree. On a binary fold and cusp, an artificial decic with a resonant unit, and two triple-lens cusps, HC seeds plus a few Newton steps recover the exact images to machine precision within the certified domain and maintain continuity under continuation. The resulting single-series templates (with (Sig_R, ρ_U) metadata) are ready for photometric and astrometric modeling.

Keywords: Gravitational microlensing (672) — Binary lens microlensing (2136) — Astrometry (80) — Photometry (1234) — High-resolution microlensing event imaging (2138)

1. INTRODUCTION

In microlensing, key observables are roots of high-degree algebraic equations; the hardest regime is near caustics where images appear and merge. Beyond quartics, radicals are unavailable in general, and global root solvers become fragile near folds and cusps. What is needed is a single, differentiable local representation with *a priori* error control across these regions. Analytic caustic expansions improve accuracy and speed (e.g. B. S. Gaudi & A. Petters 2002a,b); nonetheless, modern pipelines (e.g. VBBINARYLENSING, MULENSMODEL; (V. Bozza et al. 2018; R. Poleski & J. C. Yee 2019) remain largely global-solve based. Here we replace repeated solves by a local series with a certified radius that is uniform across folds and cusps.

The complex-analytic formulation of gravitational lensing by N point masses places the image coordinate $z = x + iy$ and the source coordinate $\zeta = \xi + i\eta$ in conjugate planes scaled by the Einstein radius of the total mass. With lens mass fractions $\{\varepsilon_j\}$ satisfying $\sum_{j=1}^N \varepsilon_j = 1$ and projected lens positions $s_j \in \mathbb{C}$, the mapping is

$$\zeta = z - \sum_{j=1}^N \frac{\varepsilon_j}{\bar{z} - \bar{s}_j}. \quad (1)$$

Eliminating \bar{z} recasts this as a single complex polynomial $P(z; \zeta, \bar{\zeta}) = 0$ whose degree is $N^2 + 1$ for generic configurations; its roots match the physical images off the caustic discriminant (P. Schneider & A. Weiss 1986; H. Asada 2009; S. H. Rhee 2003). Although the eliminant degree grows with N , the local micro-geometry is governed by the same two catastrophes (folds and cusps), so from a computational point of view catastrophe-adapted local expansions with

Email: Gleb.Berloff@warwick.ac.uk, n.g.berloff@damtp.cam.ac.uk

* Department of Physics and Astronomy

† Department of Applied Mathematics and Theoretical Physics

certified radii of convergence are strongly preferable to re-solving the full degree- $(N^2 + 1)$ polynomial at every epoch (A. O. Petters et al. 2012; H. Erdl & P. Schneider 1993).

As the source approaches a caustic, the discriminant of P vanishes and two (fold) or three (cusp) image roots coalesce. The Jacobian determinant goes to zero, point-source magnifications diverge, and global polynomial solvers become ill-conditioned. The elimination of \bar{z} also introduces extraneous roots that must be filtered (H. Asada 2009), compounding numerical fragility. A practical consequence is loss of continuity between epochs and lack of certified error control precisely where uniform accuracy is most needed (finite-source photometry, astrometric centroids, and gradient-based parameter estimation) (B. S. Gaudi & A. Petters 2002b,a; H. J. Witt & S. Mao 1994; A. Gould & C. Gaucherel 1997; V. Bozza 2010; M. Dominik 2004; A. Alexandrov & V. Zhdanov 2011). These difficulties motivate preparation-invariant, locally convergent analytic expansions capable of bridging image coalescence and enabling stable fitting. A locality preserving expansion with provable convergence and explicit parameter derivatives is therefore required. For comparison, in the weak-lensing regime, where light deflections induce small distortions in background galaxy shapes, analytic modeling has long relied on perturbative basis set frameworks and shear estimators (A. Refregier 2003a,b; S. Birrer et al. 2015). Microlensing, with its discrete image multiplicities and catastrophic behavior near caustics, has lacked an analogous, preparation-invariant analytic framework.

Recent Hyper-Catalan (HC) constructions give closed, purely algebraic series for polynomial roots (N. Wildberger & D. Rubine 2025; I. M. Gessel 2016; D. Stanton 1988). For $p(z) = \sum_{k=0}^n c_k z^k$, each root admits an ordinary power series whose coefficients are integer HC multinomials times rational functions of $\{c_k\}$. Evaluation is well-conditioned under IEEE floating point, derivatives follow termwise, and the associated characteristic system provides a certified convergence radius. In Supplementary Information we provide a Mathematica implementation of HC series for generic polynomials In Section A, and outline the geometric construction of HC coefficients and several practical advantages of their use in Section B.

We adapt HC series, Lagrange–Bürmann inversion, and parameter-dependent Weierstrass preparation to microlensing imaging polynomials. Near any multiple image (z_*, ζ_*) of multiplicity $d \geq 2$, centring and rescaling yield a monic local factor and a single “geode” variable m so that the mapping takes the Lagrange form $m = U \phi(m)$ with a preparation-invariant kernel ϕ . All d image branches follow from the one series $m(U)$ and a final single-radical lift.

We encode the local catastrophe by the unit-normalised kernel $\phi(m) = (1 - \sum_{r \geq 1} \alpha_r m^r)^{-1}$. The first nonzero $\{\alpha_r\}$ define the HC *signature*; the branch points (m^*, U^*) of $m = U \phi(m)$ and the minimal $|U^*|$ define the HC *spectrum* and radius ρ_U . These are preparation-invariant.

Two practical components follow from this geode/HC layer and form the observables of the method. First, near a fold, finite-source photometry reduces to universal one-dimensional kernels in the scaled normal offset s , with all lens dependence confined to a handful of scalars read off from the local jets and with truncation tails certified by the geode/characteristic radius. This recovers, in a parameter-explicit form, the fold kernels used to measure source size and limb darkening (M. D. Albrow et al. 2001; J. W. Blackman et al. 2020; B. S. Gaudi & A. Petters 2002a,b; H. J. Witt & S. Mao 1994; A. Gould & C. Gaucherel 1997), and because the kernels are single-series functions of s , their derivatives with respect to physical parameters remain analytic, enabling gradient-based fits and Fisher forecasts without numerical differencing. Second, the astrometric centroid is described by a single geode series that exhibits the canonical square-root approach to the fold jump and the standard cusp–triplet behaviour, again with certified tails, yielding differentiable, directly usable astrometric approaches relevant to *Gaia* (V. Belokurov & N. Evans 2002; N. Evans & V. Belokurov 2002; P. McGill et al. 2019), and in more complex binary-source or binary-lens situations where parallax and orbital motion affect astrometric paths (A. A. Nucita et al. 2016). Long-baseline surveys such as OGLE now routinely deliver thousands of microlensing events per year and have enabled population-level inferences on cold exoplanets, including the finding that wide-orbit ice giants are common (R. Poleski et al. 2021). Classical fold-crossing phenomenology and limb-darkening sensitivity in events such as OGLE-1999-BUL-23 and MACHO-97-BLG-28 can be recovered in the appropriate limits of the same HC series, while adding certified radii of convergence and an independent of global degree implementation (M. D. Albrow et al. 2001; J. W. Blackman et al. 2020). The upcoming Roman (formerly WFIRST) microlensing survey is expected to detect $\sim 10^3$ cold planets, including hundreds of sub-Earth-mass planets beyond 1 AU (M. T. Penny et al. 2019a), making fast, differentiable caustic approaches particularly valuable. Taken together, these two engines show how the same preparation-invariant Lagrange form $m = U \varphi(m)$, with its HC signature and spectrum can be applied for both photometric and astrometric microlensing.

Our paper is organized as follows. In Section 2 we review the binary-lens quintic, its global discriminant geometry, and image-track evolution away from folds and cusps. Section 3 performs the local geode preparation, derives the Lagrange

form $m = U\varphi(m)$, and presents closed HC recurrences for the coefficients M_n together with preparation-invariant formulas for the kernel coefficients α_r and certified radii from the characteristic system. Sections 4–7 present the binary-lens fold, the binary cusp, a decic lens with a resonant unit, and a physical triple-lens cusp (presented in two variants). These illustrate the multiplicity-uniform and independent of the global eliminant degree once locally prepared character of the geode construction and validate it against exact root tracking, including certified convergence radii within their analytic domains. Section 8 specializes the geode construction to the fold case ($d = 2$) and derives preparation-invariant point-source scalings, finite-source kernels, and astrometric centroids with certified truncation control from local jets. Section 9 develops the preparation-invariant classification of local microlensing behavior via the Hyper-Catalan signature and spectrum. These analytic moduli quantify the sparsity of the geode kernel, the stiffness of the local mapping, and the certified analyticity radius, thereby refining the Thom–Arnold fold/cusp taxonomy with data directly relevant to photometric and astrometric modeling. Section 10 summarizes the unified analytic framework, outlines its degree-agnostic extension to multi-point and multi-plane lenses, and discusses applications to survey constructions, model comparison, and gradient-based inference enabled by the differentiable geode/HC representation. Appendices record implementation details.

2. BINARY-LENS MAPPING, QUINTIC REDUCTION, AND ANALYTIC KINEMATICS

This section sets up the binary-lens quintic as a compact algebraic testbed and shows how Hyper-Catalan (HC) series supply not only image positions but also closed expressions for image velocities and accelerations, together with differentiable photometric and astrometric observables. The local geode/catastrophe machinery in Sections 3–9 remains the main vehicle for our fold/cusp analysis; the binary quintic here is used primarily for global kinematics, diagnostics, and validation.

Let $z = x + iy$ and $\zeta = \xi + i\eta$ denote image and source positions (angles) in units of the Einstein radius of the total mass. Align the binary along the real axis, place the secondary at $s \in \mathbb{R}$, and let $\varepsilon = m_2/(m_1 + m_2)$ be the secondary mass fraction. The standard complex lens mapping is (P. Schneider et al. 1992; K. Chang & S. Refsdal 1979, 1984; H. Witt 1990; J. H. An & N. W. Evans 2006)

$$\zeta = z - \frac{1 - \varepsilon}{\bar{z}} - \frac{\varepsilon}{\bar{z} - s}. \quad (2)$$

Eliminating \bar{z} with the conjugate of (2) yields a single complex polynomial for z whose roots coincide, with algebraic multiplicity, with the physical images away from the caustic discriminant. For a binary lens this eliminant is a quintic (P. Schneider & A. Weiss 1986; H. Witt 1990; H. J. Witt & S. Mao 1994):

$$P(z; \zeta, \bar{\zeta}; s, \varepsilon) = a_5 z^5 + a_4 z^4 + a_3 z^3 + a_2 z^2 + a_1 z + a_0 = 0, \quad (3)$$

whose coefficients are explicit polynomials in $(\zeta, \bar{\zeta})$ and the parameters (s, ε) :

$$\begin{aligned} a_5 &= \bar{\zeta}(\bar{\zeta} - s), \\ a_4 &= -s\varepsilon + (1 + 2s^2)\bar{\zeta} + s|\zeta|^2 - 2s\bar{\zeta}^2 - |\zeta|^2\bar{\zeta}, \\ a_3 &= s^2\varepsilon + s\zeta - 2|\zeta|^2 - 2s^2|\zeta|^2 + s^2\bar{\zeta}^2 + (-s^3 + 2s(\varepsilon - 1) + 2s|\zeta|^2)\bar{\zeta}, \\ a_2 &= s\varepsilon - \zeta + s^2(\varepsilon - 2)\zeta + (s^2 - 2s^2\varepsilon - s^2|\zeta|^2)\bar{\zeta} + s^3|\zeta|^2 - 2s(\varepsilon - 2)|\zeta|^2, \\ a_1 &= s(\varepsilon - 1)\left(s\varepsilon - (2 + s^2)\zeta + 2s|\zeta|^2\right), \\ a_0 &= -s^2(\varepsilon - 1)^2\zeta. \end{aligned} \quad (4)$$

The reduction (3) is algebraically equivalent to (2) wherever the Jacobian determinant

$$J(z) = 1 - \left| \frac{\partial \zeta}{\partial \bar{z}} \right|^2 = 1 - \left| \frac{1 - \varepsilon}{\bar{z}^2} + \frac{\varepsilon}{(\bar{z} - s)^2} \right|^2 \quad (5)$$

is nonzero. For generic configurations $P_z(z; \zeta, \bar{\zeta})$ is proportional to $J(z)$ up to a nonvanishing factor, so $P_z = 0$ and $J = 0$ pick out the same critical curve. The quintic P therefore provides a convenient global vehicle for resultants, discriminants, and the certified local preparations used later (H. Erdl & P. Schneider 1993; A. O. Petters et al. 2012).

Signed magnifications are $\mu_i = J(z_i)^{-1}$. The critical curve is $J = 0$; its image under (2) is the caustic (P. Schneider et al. 1992; A. O. Petters et al. 2012). Along a fold, two simple roots of P coalesce or are born into a double root; at a cusp, three simple roots coalesce or are born into a triple root. Higher multiplicities arise only on symmetry axes as enforced coincidences. These are the A_2/A_3 catastrophes whose local normal forms underlie the geode construction and the universal kernels employed later (B. S. Gaudi & A. Petters 2002a,b; A. O. Petters et al. 2012). In the linear-fold limit our local formulas reduce to the standard $u_\perp^{-1/2}$ magnification law and the $\tau^{1/2}$ centroid approach, providing a direct bridge to the canonical fold procedures (B. S. Gaudi & A. Petters 2002b,a).

Time-dependent quintic and analytic kinematics.—Let $\zeta(t)$ be any analytic source track and optionally include slow binary evolution $s(t), \varepsilon(t)$. Events such as OGLE-2015-BLG-0060, where parallax and binary orbital motion must be modelled jointly (Y. Tsapras et al. 2019), illustrate how often $s(t)$ and $\varepsilon(t)$ cannot be treated as static. On the source side, xallarap-induced distortions (e.g. OGLE-2015-BLG-0845L, where parallax and source orbital motion combine to allow a lens mass measurement) are increasingly common (Z. Hu et al. 2024). Substituting into (4) yields analytic coefficient functions $a_k(t)$ and a time-dependent quintic (where we suppressed the dependence on $\zeta, \bar{\zeta}, \varepsilon$ and s)

$$P(z, t) = \sum_{k=0}^5 a_k(t) z^k = 0. \quad (6)$$

Implicit differentiation of (6) gives closed forms for the velocity and acceleration of each image branch $z(t)$:

$$\dot{z}(t) = -\frac{P_t(z, t)}{P_z(z, t)}, \quad \ddot{z}(t) = -\frac{P_{tt} + 2P_{zt}\dot{z} + P_{zz}\dot{z}^2}{P_z} \quad \text{evaluated on } P(z, t) = 0, \quad (7)$$

where $P_z = \partial P / \partial z$, $P_t = \partial P / \partial t$, and so on, with all partials explicit polynomials in $(z, \zeta, \bar{\zeta}; s, \varepsilon)$ and their time derivatives. Because P_z vanishes only on the critical curve, (7) is well conditioned away from $J = 0$ and matches the HC-series derivatives obtained by termwise differentiation in the local charts (Section 3).

If we want to trace the roots in time, a simple and robust strategy is to recenter at the current iterate z_0 and expand

$$P(z_0 + y, t) = \sum_{j=0}^5 b_j(t; z_0) y^j, \quad b_j(t; z_0) = \sum_{k=j}^5 \binom{k}{j} a_k(t) z_0^{k-j}. \quad (8)$$

Provided $b_1 \neq 0$, the increment y admits the explicit Hyper-Catalan series in $(b_0, b_2, b_3, b_4, b_5)$:

$$y = \sum_{m_2, m_3, m_4, m_5 \geq 0} \frac{(2m_2 + 3m_3 + 4m_4 + 5m_5)!}{(1 + m_2 + 2m_3 + 3m_4 + 4m_5)! m_2! m_3! m_4! m_5!} \frac{(-b_0)^{1+m_2+2m_3+3m_4+4m_5} b_2^{m_2} b_3^{m_3} b_4^{m_4} b_5^{m_5}}{b_1^{1+2m_2+3m_3+4m_4+5m_5}}. \quad (9)$$

This is the specialisation of the general HC root series to a shifted quintic with coefficients b_j evaluated at the base point z_0 . The multi-index sum runs over all tuples (m_2, m_3, m_4, m_5) with total weight $w = 1 + m_2 + 2m_3 + 3m_4 + 4m_5$; truncation at a fixed number of terms K provides a rapidly convergent corrector. A single Newton polish on $P(z, t) = 0$ then squares the truncation error. Because the $b_j(t)$ are analytic in t , (9) differentiates termwise, giving \dot{z} and \ddot{z} as ordinary power series in the same variables; these coincide with (7) away from $J = 0$. In practice we use (7) for cheap global kinematics and the HC-differentiated series for local, certified error control near catastrophes.

At each step we evaluate the Jacobian from (5) and use the signed magnification to set the step size and to monitor physicality:

$$\Delta t = \frac{\Delta t_0}{1 + |\mu|}, \quad \mu = J(z_0)^{-1}, \quad \mathcal{R}(t) = |\zeta(z(t)) - \zeta(t)|, \quad (10)$$

with a user-chosen base step Δt_0 and a cap on $|\mu|$ near the discriminant. The residual $\mathcal{R}(t)$, computed from (2), guards against branch slips. When $b_1 \rightarrow 0$ the HC series is replaced by the geode variable m of multiplicity $d = 2$ (fold) or $d = 3$ (cusp), as developed in Section 3.

Short tracks and validation geometry.—For a concrete geometry used for illustration we reuse a wide binary with $(s, \varepsilon) = (2, 1/4)$ and two short tracks: a fold-crossing track

$$\zeta(t) = 0.30 - 0.05(t - 1)i, \quad t \in [0, 2], \quad (11)$$

and a cusp-passage track

$$\zeta(t) = t, \quad t \in [0, 1]. \quad (12)$$

Along (11) a pair is created at the entry fold, evolves inside the critical curve, and a pair of images annihilates at the exit fold. Along (12) a triple root resolves into three branches with the expected 1/3 Puiseux exponents. These tracks serve as running examples after the local geode preparation is introduced in Section 3 and will be reused in the cusp example of Section 5.

Figure 1(a) shows the caustics and the two source tracks used in (11)–(12); panels 1b–1c report the per-image magnifications $|\mu|$ versus t along the two tracks; and panels 1d–1e quantify predictor and post-Newton errors as functions of the base step Δt_0 for HC truncation orders $K \in \{1, 2, 4\}$. The observed error scaling foreshadows the certified convergence results proved in Section 3.

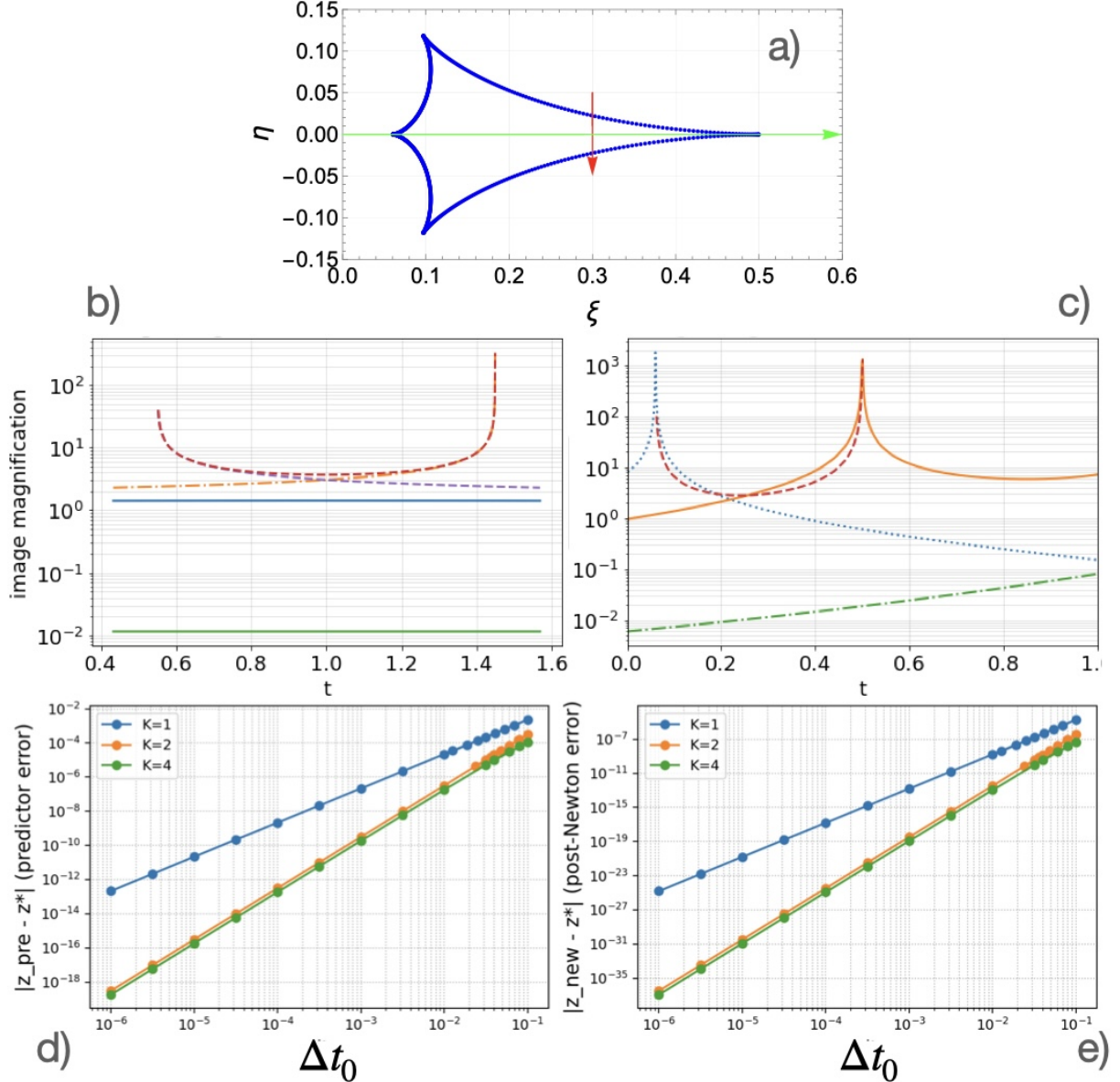


Figure 1. Binary-lens geometry at $\epsilon = 0.25$, $s = 2$. (a) Caustics with a fold-crossing track $\zeta(t) = 0.30 - 0.05(t-1)i$ (red) and a cusp-passage track $\zeta(t) = t$ (green). (b–c) Per-image magnifications along each track. (d–e) Predictor and post-Newton errors versus base step Δt_0 for HC truncation orders $K \in \{1, 2, 4\}$, showing the expected HC scaling and a quadratic reduction after one Newton step.

3. GEODE CONSTRUCTION, LAGRANGE NORMALISATION, AND HYPER–CATALAN SOLUTION

In this section we develop the core geode construction: a preparation–invariant, single–series parametrisation of all image branches that bifurcate at a multiple root of multiplicity $d \geq 2$ of the eliminated single–plane lens polynomial $P(z; \zeta, \bar{\zeta}) = 0$, with P holomorphic in z and real–analytic in $(\zeta, \bar{\zeta})$. All examples in Sections 4–7 are concrete instances of the construction introduced here. Let (z_*, ζ_*) be such a multiple image, i.e. $\partial_z^k P(z_*; \zeta_*, \bar{\zeta}_*) = 0$, $(0 \leq k < d)$, $\partial_z^d P(z_*; \zeta_*, \bar{\zeta}_*) \neq 0$.

Shift and normalisation of local coordinates.—Translate and rescale so that the multiple image sits at the origin and the pure z –jet of order d is monic:

$$z = z_* + \frac{w}{\lambda}, \quad \zeta = \zeta_* + v, \quad \bar{\zeta} = \bar{\zeta}_* + \bar{v}, \quad (13)$$

with

$$\lambda = \left[\partial_z^d P(z_*; \zeta_*, \bar{\zeta}_*) / d! \right]^{1/d}. \quad (14)$$

The normalised local polynomial

$$P_{\text{loc}}(w; v, \bar{v}) = P(z_* + w/\lambda; \zeta_* + v, \bar{\zeta}_* + \bar{v}) \quad (15)$$

is centred at $(w, v, \bar{v}) = (0, 0, 0)$ with $\partial_w^d P_{\text{loc}}(0; 0, 0) / d! = 1$, fixing the local geometric scale. From now on, all derivatives and coefficients in this section are taken in the centred, normalised coordinates of (15); for brevity we keep the notation P_{loc} to emphasise this localisation.

The steps in our local construction are at $(0, 0, 0)$. (1) Parameter-dependent Weierstrass preparation: $P_{\text{loc}}(w; v, \bar{v}) = U(t; v, \bar{v})W(t; v, \bar{v})$ with $t = w - w_c(v, \bar{v})$. (2) Geode variable $m = t^d$. (3) Cyclotomic product and square-free reduction in m . (4) Lagrange normalisation $m = U\varphi(m)$ with prepared source $U = \Lambda(v, \bar{v})$. (5) HC coefficients from φ and a certified radius from the characteristic system. (6) Lift back to images $z = z_* + (w_c + \omega m^{1/d})/\lambda$ and, if desired, polish by Newton on $W = 0$ (or $P = 0$). Next, we will explain these steps in detail.

(i) *Weierstrass preparation and centre.*—Let $t = w - w_c(v, \bar{v})$, where the *Weierstrass centre* w_c is the unique analytic germ with $w_c(0, 0) = 0$ that cancels the t^{d-1} term of the monic factor $W(t; v, \bar{v})$. By parameter-dependent Weierstrass preparation (K. Weierstrass 1879), there exist an analytic unit $\mathcal{U}(t; v, \bar{v})$ with $\mathcal{U}(0; 0, 0) \neq 0$ and a monic polynomial $W(t; v, \bar{v})$ of degree d such that

$$P_{\text{loc}}(w_c(v, \bar{v}) + t; v, \bar{v}) = \mathcal{U}(t; v, \bar{v})W(t; v, \bar{v}) = 0, \quad (16)$$

with

$$W(t; v, \bar{v}) = t^d + a_{d-2}(v, \bar{v})t^{d-2} + \cdots + a_0(v, \bar{v}), \quad [t^{d-1}]W \equiv 0, \quad a_k(0, 0) = 0. \quad (17)$$

The Weierstrass centre $w_c(v, \bar{v})$ is obtained by enforcing $\partial_w^{d-1} P_{\text{loc}}(w_c; v, \bar{v}) = 0$. We always divide the local factor by the pure t^d coefficient and choose the Weierstrass centre w_c so that $[t^{d-1}]W \equiv 0$; hence $[t^d]W \equiv 1$ and $[t^{d-1}]W \equiv 0$ by construction. In code, this should be asserted at every evaluation point. Weierstrass preparation is essential because it isolates a monic polynomial factor W in the local variable t from a nonvanishing analytic unit \mathcal{U} . Only after this factorisation does the substitution $t = \omega^j m^{1/d}$ produce a single-valued analytic function of the geode variable m ; without it, fractional powers and nonpolynomial terms in w would obstruct the construction.

(ii–iii) *Geode, cyclotomic product, and square-free reduction.*—Introduce the geode variable $m = t^d$ and set $\omega = e^{2\pi i/d}$. Form the d –fold cyclotomic product

$$R(m; v, \bar{v}) = \prod_{j=0}^{d-1} P_{\text{loc}}(w_c(v, \bar{v}) + \omega^j m^{1/d}; v, \bar{v}) = \left[\prod_{j=0}^{d-1} \mathcal{U}(\omega^j m^{1/d}; v, \bar{v}) \right] \left[\prod_{j=0}^{d-1} W(\omega^j m^{1/d}; v, \bar{v}) \right], \quad (18)$$

The first bracket is an analytic unit in m ; the second is a polynomial in m of degree d whose zeros are the geode images $m = t^d$ of the roots of $W(t; v, \bar{v}) = 0$. We also define the Weierstrass cyclotomic product

$$R_W(m; v, \bar{v}) = \prod_{j=0}^{d-1} W(\omega^j m^{1/d}; v, \bar{v}). \quad (19)$$

The substitution $t \mapsto t^d$ may introduce a parameter-uniform multiplicity in m which we now remove. Let

$$\tilde{R}(m; v, \bar{v}) = \frac{R(m; v, \bar{v})}{\gcd_m(R, \partial_m R)}, \quad \tilde{R}_W(m; v, \bar{v}) = \frac{R_W(m; v, \bar{v})}{\gcd_m(R_W, \partial_m R_W)} \quad (20)$$

with the gcd taken in the coefficients analytic in (v, \bar{v}) . For folds ($d = 2$), the cyclotomic product has the form $R \propto (m + p_0(v, \bar{v}))^2$ and hence

$$\tilde{R}_W = m + p_0(v, \bar{v}) \quad (21)$$

after dividing out the common factor. For $d \geq 3$, when the local cubic (or higher) factor W has simple roots (i.e. the discriminant $\Delta_m(R)$ does not vanish identically near $(v, \bar{v}) = (0, 0)$), R and $\partial_m R$ are generically coprime, so $\gcd_m(R, \partial_m R) = 1$ and $\tilde{R} \equiv R$ up to an analytic unit. However, special parameter values can produce an *accidental* extra factor of m in $R(m; v, \bar{v})$ (so that R and $\partial_m R$ share an m^k factor). In such cases the square-free reduction (20) cancels this extra multiplicity. An explicit example of this accidental multiplicity and its removal appears in the near-tangential triple-lens cusp of Section 7.

(iv) *Lagrange normalisation and prepared source coordinate*.—Expand the square-free Weierstrass cyclotomic product as

$$\tilde{R}_W(m; v, \bar{v}) = A(v, \bar{v})m - B(v, \bar{v}) + m^2\Psi(m; v, \bar{v}) = 0, \quad (22)$$

with $A = \partial_m \tilde{R}_W(0; v, \bar{v})$ and $B = -\tilde{R}_W(0; v, \bar{v})$, and define the prepared source coordinate

$$U = \Lambda(v, \bar{v}) = \frac{B(v, \bar{v})}{A(v, \bar{v})}. \quad (23)$$

Dividing (22) by A gives the geometric Lagrange form

$$m = U \varphi_{\text{geo}}(m, U), \quad \varphi_{\text{geo}}(m, U) = \left[1 + \frac{m \Psi(m; v, \bar{v})}{A(v, \bar{v})} \right]^{-1}. \quad (24)$$

If $d = 2$ (fold), the square-free scalar is $\tilde{R}_W(m; v, \bar{v}) = m + p_0(v, \bar{v})$, so $A \equiv 1$, $B = -p_0$ and $U = \Lambda(v, \bar{v}) = -p_0(v, \bar{v})$. Hence the geode equation is strict: $m = U$, $\varphi \equiv 1$.

(v) *Preparation-invariant kernel and Hyper-Catalan series*—Evaluate the square-free scalar at the base point $(v, \bar{v}) = (0, 0)$:

$$\tilde{R}(m; 0, 0) = \sum_{k \geq d} r_k m^k, \quad r_d \neq 0.$$

For $d \geq 3$ set

$$D(m) = \frac{\tilde{R}(m; 0, 0)}{r_d m^d} = 1 + \sum_{r \geq 1} d_r m^r, \quad d_r = [m^r](D(m) - 1), \quad (25)$$

and define the *preparation-invariant kernel*

$$\varphi(m) = \frac{1}{D(m)} = \frac{r_d m^d}{\tilde{R}(m; 0, 0)}, \quad \varphi(0) = 1. \quad (26)$$

If the cyclotomic product contributes a nonconstant pure m -unit, then $\tilde{R}(m; 0, 0) = r_d m^d \varphi(m)^{-1}$; this retains any resonances (e.g. the decic example of Section 6 with $\varphi(m) = (1 + m^7)^{-1}$). Together with the prepared source $U = \Lambda(v, \bar{v})$ this yields the *HC Lagrange form*

$$m = U \varphi(m), \quad \varphi(0) = 1, \quad (27)$$

in which U carries the *source-side* transport while φ encodes the *image-side* geometry at the base point. All preparation-dependent constants enter through Λ , not through φ .

The unique analytic germ solving (27) is the HC series

$$m(U) = \sum_{n \geq 1} M_n U^n, \quad M_n = \frac{1}{n} [w^{n-1}] \varphi(w)^n. \quad (28)$$

Writing the kernel in denominator form

$$\varphi(m) = \left(1 - \sum_{r \geq 1} \alpha_r m^r\right)^{-1} \quad (29)$$

gives the explicit Hyper–Catalan coefficients

$$M_n = \frac{1}{n} \sum_{\{k_r\} : \sum r k_r = n-1} \frac{(n + \sum k_r - 1)!}{(n-1)! \prod_r k_r!} \prod_{r \geq 1} \alpha_r^{k_r}. \quad (30)$$

Characteristic system and analyticity radius.—Branch points of $m(U)$ are critical points of (27):

$$m^* = U^* \varphi(m^*), \quad 1 = U^* \varphi'(m^*). \quad (31)$$

The analyticity radius about $U = 0$ is

$$\rho_U = \min\{|U^*| : \exists m^* \text{ satisfying (31)}\}. \quad (32)$$

Equivalently, in the Weierstrass coordinates of (16) the branch points correspond to singular solutions of the local polynomial factor $W(t^*; v^*, \bar{v}^*) = 0$, $\partial_t W(t^*; v^*, \bar{v}^*) = 0$, with $m^* = (t^*)^d$ and $U^* = \Lambda(v^*, \bar{v}^*)$. The minimal modulus $|U^*|$ among such pairs determines ρ_U .

Certified tails via a majorant kernel.—Define the nonnegative majorant kernel

$$\hat{\varphi}(m) = \left(1 - \sum_{r \geq 1} |\alpha_r| m^r\right)^{-1}, \quad (33)$$

and let $\hat{m}(U) = \sum_{n \geq 1} \hat{M}_n U^n$ solve $\hat{m} = U \hat{\varphi}(\hat{m})$ with $\hat{m}(0) = 0$. Then $\hat{M}_n \geq 0$ and $|M_n| \leq \hat{M}_n$ for all n , and for any $|U| < \hat{\rho}_U$ (the analyticity radius induced by $\hat{\varphi}$)

$$\left| m(U) - \sum_{n=1}^N M_n U^n \right| \leq \hat{m}(|U|) - \sum_{n=1}^N \hat{M}_n |U|^n. \quad (34)$$

The right-hand side is explicit once $D(m)$ (and hence the α_r) are known.

(vi) Reconstruction and practical algorithm.—Given a source offset (v, \bar{v}) near $(0, 0)$, reconstruction proceeds as follows:

- (1) Compute the prepared coordinate $U = \Lambda(v, \bar{v}) = B(v, \bar{v})/A(v, \bar{v})$ from (22).
- (2) Form the preparation–invariant kernel $\varphi(m)$ from (26) (for $d \geq 3$). For folds ($d = 2$) use the linear kernel obtained directly from (21).
- (3) Evaluate the geode series $m(U) = \sum_{n \geq 1} M_n U^n$ via (30), truncating at order K and using (34) to certify the truncation error.
- (4) Lift to d geode seeds $t_k^{(0)} = \omega^k m^{1/d}$ with $\omega^d = 1$. For $d = 3$ the monic Weierstrass factor takes the depressed form

$$W(t; v, \bar{v}) = t^3 + p(v, \bar{v}) t + q(v, \bar{v}), \quad [t^3]W \equiv 1, \quad [t^2]W \equiv 0. \quad (35)$$

When the skewness $S = |p|/|m|^{2/3}$ is not small, the three naive lifts $t_k^{(0)} = \omega^k m^{1/3}$ can lie in the same Newton basin and polish to a single branch. A robust fix is to use the first Cardano correction,

$$t_k^{(1)} = \omega^k m^{1/3} - \frac{p}{3\omega^k m^{1/3}}, \quad k = 0, 1, 2, \quad (36)$$

which is exactly the one-step Newton update for $t^3 + pt + q = 0$ linearized about $t = \omega^k m^{1/3}$.

- (5) (Optional) Refine each seed by Newton iteration on the centred Weierstrass factor $W(t; v, \bar{v}) = 0$ to obtain the exact local roots t_k .

(6) Map back to the physical image plane via

$$z = z_* + \frac{w_c(v, \bar{v}) + t_k}{\lambda},$$

and, if desired, perform the final Newton polish on the full eliminated equation $P(z; \zeta, \bar{\zeta}) = 0$ as a global consistency check.

Thus the HC series provides analytic seeds, while the exact images are recovered by a short, stable Newton solve on $W = 0$ (or P). The construction cleanly separates preparation-dependent data (W, w_c, Λ) from preparation-invariant objects $(\varphi, \{\alpha_r\}, \{M_n\}, \rho_U)$, with φ computed solely from the square-free scalar $\tilde{R}(m; 0, 0)$.

Remark on roots collapse.—The geode lift $t \sim \omega m^{1/3}$ is only the leading term of the local expansion for each branch of a cusp. If the geometric coefficients $\{p, q\}$ in the monic cubic $W = t^3 + pt + q$ are not small relative to $m^{2/3}$ and m , two of the true roots may sit well outside the circle $|t| = |m|^{1/3}$. In that regime the naive seeds $t_k^{(0)} = \omega^k m^{1/3}$ may lie in the same Newton basin (near the small- $|t|$ root) and hence “collapse” under Newton iteration. Adding the $O(p/m^{1/3})$ correction in (36) restores the correct basins while preserving the preparation-invariant Lagrange map $m = U\varphi(m)$.

Universality and link to examples.—The construction applies to any analytic lens polynomial with a finite-multiplicity image: all local behaviour is captured by $m = U\varphi(m)$. The intrinsic data are $\{\alpha_r\}$ and ρ_U ; preparation-dependent choices appear only through Λ . Sections 4–7 illustrate folds, binary cusps, a resonant decic, and triple-lens cusps. Notations and symbols used are presented in the Supplementary Information in Section C for a quick reference.

4. ARTIFICIAL QUINTIC WITH A FOLD

This example implements the full geode construction in the simplest fold case ($d = 2$), where the preparation-invariant kernel is trivial, $\varphi \equiv 1$. It therefore isolates, in a transparent setting, centering and local normalisation, geode elimination, Lagrange normalisation, certified analyticity radius, and Newton polish.

Consider

$$P(z, \zeta) = z^5 + z^2 + \zeta(z^3 + z + 1). \quad (37)$$

At $(z, \zeta) = (0, 0)$ there is a multiple image of multiplicity $d = 2$ since $P(z, 0) = z^2(z^3 + 1)$. We work at the base point $(z_*, \zeta_*) = (0, 0)$ and scale λ as in (14); here $\lambda = 1$ since $\partial_z^2 P(0; 0)/2! = 1$.

(i) *Local normalisation and centre $z_c(\zeta)$.*—Set $z = z_c(\zeta) + t$ and choose $z_c(\zeta)$ so that the linear term in t vanishes: $[t^1] P(z_c(\zeta) + t, \zeta) = 0$. Expanding in ζ around $\zeta = 0$ gives the centred image position

$$z_c(\zeta) = -\frac{1}{2}\zeta - \frac{3}{8}\zeta^3 - \frac{5}{32}\zeta^4 + O(\zeta^5). \quad (38)$$

For a quadratic Weierstrass factor $W = t^2 + p_0(\zeta)$ one can express $z_c(\zeta)$ and $p_0(\zeta)$ in terms of $P(0, \zeta)$, $P_z(0, \zeta)$, and $P_{zz}(0, \zeta)$ via

$$z_c(\zeta) = -\frac{P_z(0, \zeta)}{P_{zz}(0, \zeta)} + O(\zeta^2), \quad p_0(\zeta) = \frac{P(0, \zeta)}{P_{zz}(0, \zeta)} - \frac{P_z(0, \zeta)^2}{4P_{zz}(0, \zeta)^2} + O(\zeta^2), \quad (39)$$

which, in this example, reduce to the explicit series (38) and (40) below.

(ii-iii) *Monic Weierstrass factor, geode, and square-free eliminant.*—Dividing by the t^2 -coefficient yields the monic Weierstrass factor

$$W(t, \zeta) = t^2 + p_0(\zeta), \quad p_0(\zeta) = -\zeta + \frac{1}{4}\zeta^2 - \frac{3}{2}\zeta^3 - \frac{3}{4}\zeta^4 + O(\zeta^5). \quad (40)$$

Introduce the geode $m = t^2$ to symmetrise the two branches. The $d = 2$ cyclotomic product

$$R(m, \zeta) = \prod_{j=0}^1 P(z_c(\zeta) + \omega^j m^{1/2}, \zeta), \quad \omega^2 = 1, \quad (41)$$

factorises as

$$R(m, \zeta) = \mathcal{U}(m, \zeta) (m + p_0(\zeta))^2, \quad \mathcal{U}(m, \zeta) = \mathcal{U}(\sqrt{m}, \zeta) \mathcal{U}(-\sqrt{m}, \zeta), \quad \mathcal{U}(0, 0) \neq 0, \quad (42)$$

where \mathcal{U} is the analytic Weierstrass unit. For folds, the pure m -part of \mathcal{U} at the base point is constant, so it does not enter the kernel. Removing the parameter-uniform multiplicity introduced by $m = t^2$ gives the square-free eliminant

$$\tilde{R}_W(m, \zeta) = m + p_0(\zeta) = 0. \quad (43)$$

(iv) *Canonical fold Lagrange form and kernel $\varphi \equiv 1$.*—Equation (43) is already in Lagrange form

$$m = U \varphi(m), \quad U = \Lambda(\zeta) = -p_0(\zeta), \quad \varphi(m) \equiv 1, \quad \varphi(0) = 1. \quad (44)$$

Thus the preparation–invariant kernel is strict, with no resonant unit: $\alpha_r \equiv 0$ and the HC series collapses to $m(U) = U$ exactly. In terms of the source coordinate, $m(\zeta) = -p_0(\zeta)$, and the two local images are $t_{\pm} = \pm m^{1/2}$. In the classification language of Section 9, this corresponds to an HC signature with multiplicity $d = 2$ and no nonzero kernel coefficients, i.e. a canonical fold with trivial kernel.

(v) *Seeds, Newton polish, and lift.*—Use geode seeds $t_{\pm}^{(0)} = \pm m^{1/2}$ and refine them by Newton’s method on the well-conditioned quadratic $W = t^2 + p_0$:

$$t \leftarrow t - \frac{W(t, \zeta)}{\partial_t W(t, \zeta)} = t - \frac{t^2 + p_0(\zeta)}{2t}. \quad (45)$$

In implementation, one guards this update for very small $|t|$ (or directly uses the exact quadratic root $t = \pm\sqrt{-p_0}$) to avoid division by $2t$. Undoing the shift (and scale) gives the images

$$z(\zeta) = z_* + z_c(\zeta) + t(\zeta), \quad (\lambda = 1). \quad (46)$$

Thus the HC series supplies analytic seeds and the exact images are obtained by a single, stable Newton polish on $W = 0$.

(vi) *Certified analyticity radius.*—Because the Weierstrass unit is nonvanishing, the systems $(P, P_z) = (0, 0)$ and $(W, W_t) = (0, 0)$ are equivalent; we use (P, P_z) for convenience. From

$$P_z(t, \zeta) = 5t^4 + 2t + \zeta(3t^2 + 1) = 0 \Rightarrow \zeta(t) = -\frac{5t^4 + 2t}{3t^2 + 1}, \quad (47)$$

eliminating ζ from $P = 0$ and $P_z = 0$ (e.g. via the resultant in ζ) yields the critical equation

$$2 + t + 4t^3 + 4t^4 + 2t^6 = 0. \quad (48)$$

Its nearest roots t^* map by (47) to

$$\zeta^* \approx -0.0230696 \pm 0.2700834i, \quad \rho_{\zeta} = \min |\zeta^*| \approx 0.271. \quad (49)$$

Hence the local series $m(\zeta)$ (and thus $t(\zeta)$) converge for $|\zeta| < \rho_{\zeta}$. Since $U = \Lambda(\zeta) = -p_0(\zeta)$ and $\Lambda'(0) \neq 0$, the corresponding analyticity radius in the source coordinate satisfies $\rho_U \sim |\Lambda'(0)| \rho_{\zeta}$ near the base point, in agreement with the general characteristic–radius discussion of Section 3. Cauchy majorants give explicit tail bounds at any $r \in (|\zeta|, \rho_{\zeta})$, and one Newton update on W squares the geode seed error.

Numerical check at $\zeta = 0.01$.—From (38) and (40):

$$z_c(0.01) = -5.000377 \times 10^{-3}, \quad p_0(0.01) = 9.976508 \times 10^{-3}, \quad t_{\pm}^{(0)} = \pm i 9.988247 \times 10^{-2}.$$

Thus

$$z_{\pm}^{(0)} = z_c(0.01) + t_{\pm}^{(0)} = -5.000377 \times 10^{-3} \pm i 9.988247 \times 10^{-2}.$$

One Newton step using (45) already reduces the residuals $|P(z_{\pm}, 0.01)|$ to the 10^{-3} level; in practice a second Newton step drives the residuals to machine precision at $|\zeta| = 0.01 \ll \rho_{\zeta}$.

This example realises the general scheme with $d = 2$, $m(U) = U = -p_0(\zeta)$, and trivial kernel $\varphi \equiv 1$. Figure 2(a) shows the two image branches as ζ is varied along the real axis. Solid curves (geode + Newton on W) and dashed curves (direct root solving) agree to within numerical precision throughout $|\zeta| \lesssim 0.6$. Within the certified radius $|\zeta| < \rho_{\zeta} \approx 0.271$ this agreement is guaranteed by the characteristic–radius analysis, and the numerical performance remains excellent even somewhat beyond this domain.

5. BINARY-LENS CUSP (PHYSICAL QUINTIC)

We now apply the geode construction to a physical binary-lens cusp. For the binary with $(s, \varepsilon) = (2, 1/4)$ the single-plane eliminant $P(z; \zeta, \bar{\zeta})$ has a triple image ($d = 3$) at $(\zeta_*, z_*) = (0.0603074, -0.8793852)$, corresponding to a cusp on the central caustic. For notational simplicity, we will assume the source track is along the the real axis, so $\zeta = \bar{\zeta}$. Following the construction of Section 3, we translate and scale

$$z = z_* + \frac{w}{\lambda}, \quad \zeta = \zeta_* + u, \quad P_{\text{loc}}(w; u) = P(z_* + w/\lambda; \zeta_* + u), \quad (50)$$

with λ chosen so that the pure w -jet is monic (Eq. (14)), so $\lambda = [\partial_z^3 P(z_*; \zeta_*)/3!]^{1/3} = -0.8398545975895852$. This sets $\partial_w^3 P_{\text{loc}}(0; 0)/3! = 1$ and fixes the local scale.

(i) *Weierstrass centre and monic factor*.—Let $t = w - w_c(u)$; the Weierstrass centre $w_c(u)$ is the unique analytic germ with $\partial_w^2 P_{\text{loc}}(w_c(u); u) = 0$ and $w_c(0) = 0$. Solving order by order in u gives

$$w_c(u) = -35.2886u + 518.743u^2 - 12003.3u^3 + 43246.5u^4 + O(u^5). \quad (51)$$

By parameter-dependent Weierstrass preparation,

$$P_{\text{loc}}(w_c(u) + t; u) = \mathcal{U}(t, u) W(t, u), \quad W(t, u) = t^3 + p(u)t + q(u), \quad p(0) = q(0) = 0, \quad (52)$$

with $\mathcal{U}(0, 0) \neq 0$ and a depressed ($[t^2]W = 0$) monic cubic W . This is the $d = 3$ specialisation of the general preparation (16).

(ii–iii) *Geode, cyclotomic product, and square-free scalar*.—Introduce the cusp geode $m = t^3$ and $\omega = e^{2\pi i/3}$. The cyclotomic product removes fractional powers and is analytic in m ,

$$\tilde{R}_W(m; u) = R_W(m; u) = \prod_{j=0}^2 W(\omega^j m^{1/3}; u). \quad (53)$$

(iv) *Prepared source and geometric Lagrange form*.—Expand the square-free scalar associated with the local cubic factor W as

$$\tilde{R}_W(m; u) = A(u)m - B(u) + m^2\Psi(m; u), \quad A(u) = \partial_m \tilde{R}_W(0; u), \quad B(u) = -\tilde{R}_W(0; u), \quad (54)$$

and define the prepared source

$$U = \Lambda(u) = \frac{B(u)}{A(u)} = 42394.0757u^3 + O(u^4). \quad (55)$$

This $U(u)$ parameterises the exact geometric transport for our chosen preparation: dividing (54) by $A(u)$ gives the geometric Lagrange form $m = U \varphi_{\text{geo}}(m, U)$, $\varphi_{\text{geo}}(m, U) = \left(1 + \frac{m\Psi(m; u)}{A(u)}\right)^{-1}$, with u regarded as a function of U via (55).

(v) *Preparation-invariant kernel φ , HC series, and radius*.—Independently of this geometric transport, the preparation-invariant kernel used for HC seeds is obtained from the full imaging polynomial P by forming its cyclotomic product in the geode variable m and then taking the square-free scalar at the base point ($u = 0$). For the present binary-lens cusp this yields the pure m -jet

$$\tilde{R}(m; 0) = m^3 [1 - \alpha_1 m - \alpha_2 m^2],$$

so the preparation-invariant kernel is $\varphi(m) = (1 - \alpha_1 m - \alpha_2 m^2)^{-1}$, $\varphi(0) = 1$, with $\alpha_1 = -0.4203353$, $\alpha_2 = -0.0219406$, $\alpha_{r \geq 3} = 0$. In the HC classification of Section 9, this cusp has signature $\text{Sig}_R = (3; \alpha_1, \alpha_2)$.

For this binary example the cyclotomic unit from the full P does not carry any nontrivial m -dependence at the base point, so \tilde{R}_W and \tilde{R} agree up to an analytic unit and the geometric kernel φ_{geo} and preparation-invariant kernel φ coincide at $(m, U) = (0, 0)$. In higher-degree cases (e.g. the decic cusp with a resonant unit in Section 6) the cyclotomic product of the full P does contribute a nontrivial pure m -unit, and the preparation-invariant kernel φ must be computed from this full square-free scalar rather than from the cubic factor alone.

With the quadratic kernel $\varphi(m)$, only α_1 and α_2 enter the HC recurrences. Specialising (30) to this case gives

$$M_n = \frac{1}{n} \sum_{k_2=0}^{\lfloor (n-1)/2 \rfloor} \frac{(2(n-1)-k_2)!}{(n-1)! ((n-1)-2k_2)! k_2!} \alpha_1^{n-1-2k_2} \alpha_2^{k_2}, \quad n \geq 1,$$

and the geode series

$$m(U) = \sum_{n \geq 1} M_n U^n.$$

For truncation control we use the nonnegative majorant kernel $\widehat{\varphi}(m) = (1 - |\alpha_1|m - |\alpha_2|m^2)^{-1}$, which induces $\widehat{m}(U) = \sum \widehat{M}_n U^n$ with $\widehat{M}_n \geq 0$ and $|M_n| \leq \widehat{M}_n$. The majorant characteristic equation $3|\alpha_2|m^2 + 2|\alpha_1|m - 1 = 0$ has a positive root \widehat{m}^* , and the corresponding certified radius $\widehat{\rho}_U = \widehat{m}^*(1 - |\alpha_1|\widehat{m}^* - |\alpha_2|(\widehat{m}^*)^2) = 0.5622011$ is a direct specialisation of the general characteristic–radius formula (32).

(vi) *Reconstruction at $u = 0.01$ and Newton polish.*—To reconstruct images at a specific source position we use the practical algorithm of Section 3. For $u = 0.01$ the exact Weierstrass centre, obtained by solving $\partial_w^2 P_{\text{loc}}(w; u) = 0$, is $w_c(0.01) = -0.3139924$. For comparison, the truncated series (51) gives $w_c(0.01) \approx -0.312582$. At this centre define $f(t; u) = P_{\text{loc}}(w_c(u) + t; u)$ and evaluate $f_0 = f(0; u)$, $f_1 = \partial_t f(0; u)$, $f_3 = \frac{1}{6} \partial_t^3 f(0; u)$ at $u = 0.01$, obtaining $f_0 = -0.076677$, $f_1 = 0.1752943$, $f_3 = 0.4313251$. Hence the prepared source

$$U = \frac{B(u)}{A(u)} = -\frac{f_0^3}{3f_0^2 f_3 + f_1^3} = 0.0346934.$$

(Using the full $U(u)$ expression (55) yields $U \approx 0.0342434$.)

Solving the cubic $-\alpha_2 m^3 - \alpha_1 m^2 + m - U = 0$ for m at this U gives $m = 0.0342009$. Lifting to geode seeds t_k with Cardano correction Eq. (36) gives

$$t_k = \{0.310598 - 0.477264 i, -0.406215 + 0.193705 i, 0.0956164 + 0.283559 i\}. \quad (56)$$

Mapping back to the physical image plane by $z = z_* + (w_c(u) + t_k)/\lambda$ and performing six Newton polish steps gives the three images at $u = 0.01$ to machine accuracy.

This binary–lens cusp realises the geode construction for $d = 3$ with a nontrivial kernel $\varphi(m) = (1 - \alpha_1 m - \alpha_2 m^2)^{-1}$ and HC signature $\text{Sig}_R = (3; \alpha_1, \alpha_2)$. The prepared source $U(u)$ plays the role of the local control parameter; the HC series $m(U)$ provides analytic seeds with certified radius $|U| \leq \widehat{\rho}_U$; Newton on the centred cubic $W(t, u)$ yields the exact images; and the lift $z = z_* + (w_c(u) + \omega m^{1/3})/\lambda$ reconstructs the three branches. The full evolution of these images as the source moves along the real axis is shown in Figure 2(b). Solid curves (HC + Newton on W) and dashed curves (direct numerical solutions of P) are indistinguishable within the certified domain $|U(u)| \leq \widehat{\rho}_U$, including the neighbourhood of the cusp where the three branches coalesce. This cusp illustrates the universal behavior predicted by catastrophe theory and confirmed in observational modeling of quasar microlensing caustic crossings (V. Shalyapin et al. 2002). Our framework generalizes such approaches to degree–agnostic analytic representations. Together with Example 4, this demonstrates how the same local geode framework accommodates both folds and cusps in physical binary lenses.

6. DECIC CUSP WITH A RESONANT UNIT

Our third example is a cusp whose eliminated polynomial is of degree ten and carries a nontrivial *resonant unit* in the geode variable. It provides a clean test of the HC construction in a higher–degree setting with a nontrivial kernel.

Consider

$$P(z, \zeta) = z^{10} + z^3 + \zeta(1 + z + z^7 + z^8). \quad (57)$$

At $\zeta = 0$ there is a triple image at $z_* = 0$ ($d = 3$), since $P(z, 0) = z^3(1 + z^7)$. With $z = t$ and unit scaling $\lambda = 1$ the local Weierstrass preparation takes the simple form

$$P_{\text{loc}}(t, \zeta) = \mathcal{U}(t, \zeta) W(t, \zeta), \quad \mathcal{U}(t, \zeta) = 1 + t^7, \quad W(t, \zeta) = t^3 + \zeta(1 + t), \quad (58)$$

so $z_c \equiv 0$ and W is already a depressed cubic.

(ii–iii) *Geode, cyclotomic product, and square–free scalar.*—Set the cusp geode $m = t^3$ and $\omega = e^{2\pi i/3}$. The three–fold cyclotomic product is

$$R(m, \zeta) = \prod_{j=0}^2 P(\omega^j m^{1/3}, \zeta) = \left[(m + \zeta)^3 + \zeta^3 m \right] (1 + m^7), \quad (59)$$

where the bracket arises from the cubic factor W and the unit $1 + m^7$ comes from the cyclotomic product of \mathcal{U} . Near $(m, \zeta) = (0, 0)$ one has $\text{gcd}_m(R, \partial_m R) = 1$, so the square–free scalar is $\tilde{R}(m, \zeta) \equiv R(m, \zeta)$ up to a nonzero constant factor.

(iv) *Geometric transport.*—Write the geometric bracket in (59) as

$$(m + \zeta)^3 + \zeta^3 m = A(\zeta) m - B(\zeta) + m^2 \Psi(m, \zeta), \quad A(\zeta) = \zeta^2(3 + \zeta), \quad B(\zeta) = -\zeta^3, \quad \Psi(m, \zeta) = m + 3\zeta. \quad (60)$$

The prepared source coordinate is

$$U = \Lambda(\zeta) = \frac{B(\zeta)}{A(\zeta)} = -\frac{\zeta}{3 + \zeta}, \quad (61)$$

which behaves as $U \sim -\zeta/3$ near $\zeta = 0$. Then the *exact geometric transport* identity obtained from $A m - B + m^2 \Psi = 0$ is

$$U = m \left(1 + \frac{m \Psi(m, \zeta)}{A(\zeta)} \right) = m + \frac{m^2 (m + 3\zeta)}{\zeta^2(3 + \zeta)} \iff m = U \varphi_{\text{geo}}(m, \zeta), \quad \varphi_{\text{geo}}(m, \zeta) = \left(1 + \frac{m \Psi}{A} \right)^{-1}. \quad (62)$$

The kernel φ_{geo} encodes the exact m – U relation for this decic, but depends explicitly on ζ and is not preparation–invariant.

(v) *Preparation–invariant kernel φ , resonant unit, and HC seeds.*—Independently of the geometric transport (62), the preparation–invariant kernel that drives the HC seeds is obtained at the base point from the square–free scalar:

$$\tilde{R}(m; 0) = m^3(1 + m^7) \Rightarrow r_3 = [m^3] \tilde{R} = 1, \quad \varphi(m) = \frac{r_3 m^3}{\tilde{R}(m; 0)} = \frac{1}{1 + m^7}. \quad (63)$$

Thus φ records the *resonant unit* $1 + m^7$ coming from the cyclotomic product; it is *not* the full geometric kernel φ_{geo} in (62). In the HC classification of Section 9, this cusp has signature

$$\text{Sig}_R = (3; \alpha_7), \quad \alpha_7 = -1, \quad \alpha_{r \neq 7} = 0, \quad (64)$$

reflecting the seven–fold resonance in the kernel.

Let $m(U) = \sum_{n \geq 1} M_n U^n$ solve $m = U \varphi(m)$ with φ from (63). By Lagrange–Bürmann,

$$M_n = \frac{1}{n} [w^{n-1}] \varphi(w)^n = \frac{1}{n} [w^{n-1}] (1 + w^7)^{-n},$$

so M_n vanishes unless $n \equiv 1 \pmod{7}$. Explicitly,

$$M_n = \begin{cases} (-1)^k \frac{1}{7k+1} \binom{8k}{k}, & n = 7k+1, \\ 0, & n \not\equiv 1 \pmod{7}, \end{cases} \quad m(U) = U - U^8 + 8U^{15} - 92U^{22} + 1240U^{29} - \dots. \quad (65)$$

This HC series furnishes analytic *seeds*; the exact geometric transport is restored using (62) after lifting to t and polishing on $W = 0$.

Characteristic system and seed analyticity radius.—Branch points of the seed map $m(U)$ satisfy

$$m^* = U^* \varphi(m^*), \quad 1 = U^* \varphi'(m^*) \iff \varphi(m^*) - m^* \varphi'(m^*) = 0.$$

For $\varphi(m) = (1 + m^7)^{-1}$ we have

$$\varphi'(m) = -\frac{7m^6}{(1 + m^7)^2}, \quad \Delta(m) = \varphi(m) - m\varphi'(m) = \frac{1 + 8m^7}{(1 + m^7)^2}.$$

Thus branch points satisfy $1 + 8m^7 = 0$, i.e. $m^7 = -1/8$, so $|m_*| = (1/8)^{1/7}$. The corresponding control values are

$$U_* = \frac{m_*}{\varphi(m_*)} = m_*(1 + m_*^7) = m_* \left(1 - \frac{1}{8}\right) = \frac{7}{8}m_*,$$

and the analyticity radius of the HC seed series is therefore $\rho_U = \min |U_*| = \frac{7}{8} \left(\frac{1}{8}\right)^{1/7} \simeq 0.6506$. In practice the usable domain is further constrained by the source transport $U = \Lambda(\zeta) = -\zeta/(3 + \zeta)$ and by proximity to the actual cusp in the ζ -plane (see Figure 2(c)).

Reconstruction (practical route).—Reconstruction in this example follows the general recipe:

1. Given ζ , compute the prepared source $U = \Lambda(\zeta) = -\zeta/(3 + \zeta)$.
2. Evaluate the HC seed $m(U)$ from (65), truncating at $|U| < \rho_U$ and using the sparsity pattern $n = 7k + 1$.
3. Lift to cubic seeds $t_k^{(0)} = \omega^k m(U)^{1/3}$, $k = 0, 1, 2$.
4. Enforce the exact relation by Newton iteration on the centred factor $W(t, \zeta) = t^3 + \zeta(1 + t)$:

$$t \leftarrow t - \frac{W(t, \zeta)}{3t^2 + \zeta}.$$

5. Output images $z = t$ (since $z_c \equiv 0$). Error transport from m to t obeys

$$|\delta t^{(0)}| \leq \frac{1}{3} |m|^{-2/3} |\delta m|,$$

and Newton converges quadratically whenever $3t^2 + \zeta \neq 0$.

Here the resonant unit $1 + m^7$ affects only the seed kernel φ ; the ζ -dependence enters via the analytic transport and the cubic W , on which Newton gives quadratic convergence. Figure 2(c) shows the ten roots of the decic as ζ varies along the real axis. The coloured solid curves (HC seeds + Newton polish on W) reproduce the three physical branches emanating from the cusp and lie directly atop the numerically exact root tracks (black dashed curves), up to the analyticity boundary set by ρ_U . This demonstrates that the HC geode framework remains stable, accurate, and degree-agnostic even in the presence of a nontrivial resonant kernel.

7. TRIPLE – LENS CUSP (PHYSICAL DECIC, LOCAL CUBIC)

Our final examples apply the geode/HC construction to a fully physical three-point-mass lens, where the global lens mapping is non-holomorphic in z but the local imaging polynomial near a cusp is still captured by the same preparation-invariant construction. We consider two variants of the triple-lens cusp: a straightforward application of the geode method and a configuration that is geometrically extreme: the source trajectory grazes the caustic almost tangentially, making it one of the hardest cases for traditional root-tracking schemes. We treat two variants with the same masses $\varepsilon = (\frac{1}{2}, \frac{3}{10}, \frac{1}{5})$ but different positions $s = (0, 1, 1 + 3i)$ and $s = (0, 1, (1 + i)/2)$; Figures 3(a,b) mark the analysed cusps (red dots).

We consider the Einstein-scaled three-point-mass lens

$$\zeta = z - \sum_{j=1}^3 \frac{\varepsilon_j}{\bar{z} - \bar{s}_j}. \quad (66)$$

The corresponding caustic networks are plotted in Figures 3(a-b).

First, we will analyze the triple-lens cusp with $(s_1, s_2, s_3) = (0, 1, 1 + 3i)$ (see Fig. 3(a)). The cusp (red dot in Fig. 3(a)) is given by

$$z_* = 0.7803934 - 0.3667703i, \quad \zeta_* = 0.6199736 + 0.5411154i. \quad (67)$$

Section D of the Supplementary Information gives the details of the construction of the geode and HC series that follow the method we described in Sec. 3. Here we only provide the outline of the construction.

After local normalization and shift we consider the normalised local imaging polynomial

$$P_{\text{loc}}(w; v, \bar{v}) = P(z_* + w/\lambda; \zeta_* + v, \bar{\zeta}_* + \bar{v}), \quad (68)$$

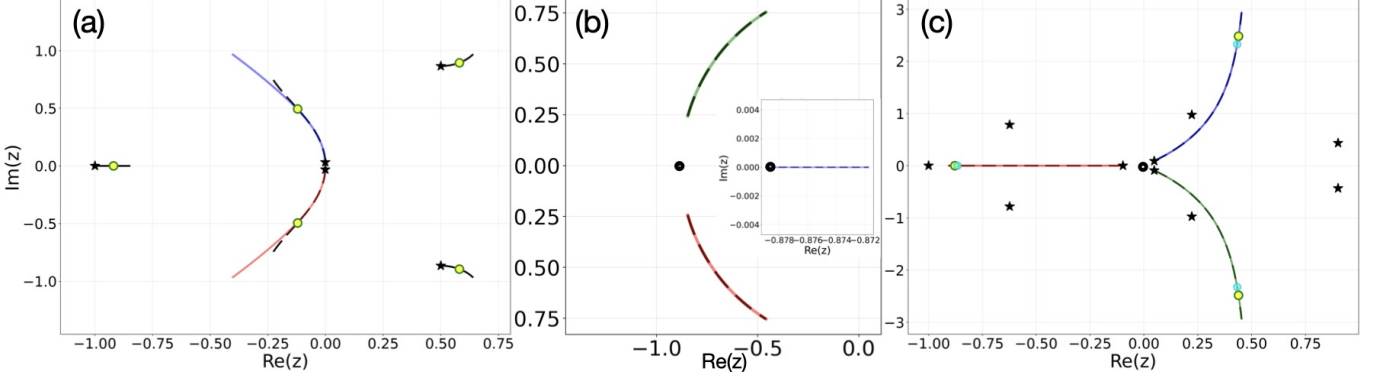


Figure 2. Root trajectories for three polynomial systems as the parameter ζ (or $u = \zeta - \zeta_*$) varies. (a) **Quintic fold** given by Eq. 37. Black stars mark the roots at $\zeta \approx 0$. Solid coloured curves (blue/red) show geode approximations valid up to $\zeta = 0.6$. Black dashed lines indicate numerically exact roots extending to $\zeta = 0.8$. Yellow-green circles mark the convergence radius $\rho_\zeta \approx 0.271$. (b) **Binary-lens cusp** considered in Section 5 emanating from (z_*, ζ_*) . Three image branches (coloured solid: geode; black dashed: exact) are tracked from the cusp singularity as the parameter u increases until $|U(u)|$ reaches the certified radius $\hat{\rho}_U$. The black filled circle marks the cusp point. Inset: zoomed view of the local structure near the cusp with the third image trajectory too short to be visible on the main plot. (c) **Decic polynomial** (given by Eq. 57). Black stars correspond to all ten roots at $\zeta \approx 0$. Coloured solid curves show the HC series combined with Newton polishing for the triple image. Black dashed lines show the exact roots trajectories emanating from the cusp. Cyan circles mark the safe radius ($0.95 \rho_U$) where continuation begins, while yellow-green circles denote the convergence radius ρ_U . HC seeds from the unit-aware kernel $\varphi(m) = (1 + m^7)^{-1}$ are used only for $|U| < 0.95 \rho_U$ with $\rho_U \simeq 0.651$; beyond this limit a predictor-corrector continuation uses the previous polished roots as seeds. All three panels demonstrate geode-based root tracking with high accuracy within their certified radii of convergence.

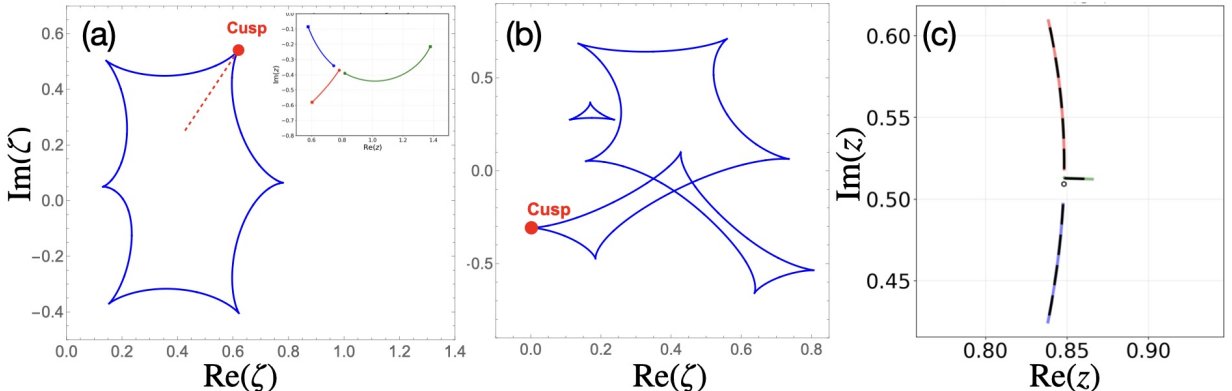


Figure 3. Caustic structure and image trajectories for two triple-lens configurations. (a,b) Source-plane caustics for a triple lens with mass fractions $\varepsilon = (\frac{1}{2}, \frac{3}{10}, \frac{1}{5})$ at positions $s = (0, 1, 1 + 3i)$ (a) and $s = (0, 1, \frac{1+i}{2})$ (b). The analysed cusp is marked by the red dot; the red dashed segment indicates the initial source direction (too short to be visible in (b)). **Inset in (a):** image trajectories ($\text{Im } z$ vs. $\text{Re } z$) for the short track $\zeta = \zeta_* - (2 + 3i)u$, $u \in [0.001, 0.1]$, reconstructed by the local geode construction: evaluate the HC series $m(U)$ from the preparation-invariant kernel φ , lift per branch $t = \omega m^{1/3}$ (with anisotropic seeds), and apply a short Newton polish on the full eliminated decic $P(z; \zeta, \bar{\zeta}) = 0$. Coloured solid curves: geode+Newton; black dashed curves: exact roots of $P(z; \zeta, \bar{\zeta}) = 0$. (c) Near-tangential cusp passage for the configuration in (b): image trajectories as the source moves along the real axis from $u = 5 \times 10^{-4}$ to 0.033. The same HC geode → lift → Newton construction recovers all three branches with machine-precision residuals; the apparent “jump” in one branch is a projection effect from crossing a nearby fold: continuation in the geode variable remains single-valued and smooth (Sec. 7).

centred at $(w, v, \bar{v}) = (0, 0, 0)$ with $\partial_w^3 P_{\text{loc}}(0; 0, 0)/3! = 1$ (ensured by $\lambda = 3.179048207371207 - 0.970805399048372i$). The Weierstrass centre $w_c(v, \bar{v})$ defined by $\partial_w^2 P_{\text{loc}}(w_c(v, \bar{v}); v, \bar{v}) = 0$, $w_c(0, 0) = 0$, is given by

$$w_c(v, \bar{v}) = (-0.6830560 - 1.404901i)v - (4.216304 + 2.530664i)\bar{v} + O(\|(v, \bar{v})\|^2). \quad (69)$$

The preparation–invariant Lagrange form is $m = U\varphi(m)$ where

$$\varphi(m) = (1 - \alpha_1 m - \alpha_2 m^2 - \alpha_3 m^3 - \alpha_4 m^4)^{-1}, \quad (70)$$

with $\alpha_1 = -(0.130049 + 0.105168 i)$, $\alpha_2 = (0.00357267 - 0.00154033 i)$, $\alpha_3 = 0.0000814471 + 0.0000559569 i$ and $\alpha_4 = 1.21561 \cdot 10^{-6}$, where we neglected the terms below 10^{-6} . In the HC language of Section 9 this example has signature $\text{Sig}_R = (3; \alpha_1, \alpha_2, \alpha_3, \alpha_4)$.

The inset of Fig. 3(a) shows three tracks emanating from the cusp along the source trajectory given by $\zeta = \zeta_* - (2 + 3i)u$. For $u = 0.01$, we get $U = -0.00125007 - 0.00388306 i$ and $m(u) = -0.00124729 - 0.0038829 i$ from HC series. The lifted roots are $t_k = (0.310598 - 0.477264 i, -0.406215 + 0.193705 i, 0.0956164 + 0.283559 i)$ and six steps of Newton polish bring the solutions to seven significant digits as $z_{1,2,3} = (0.9242055 - 0.4303363 i, 0.6873154 - 0.2815570 i, 0.7720886 - 0.3837485 i)$.

For our second variety of the triple lens we consider $(s_1, s_2, s_3) = (0, 1, \frac{1+i}{2})$ with the cusp at

$$z_* = 0.8480548 + 0.5093864 i, \quad \zeta_* = 0.001904246 - 0.3071656 i, \quad (71)$$

with cubic scale (pure w –jet monic)

$$\lambda = \left[\partial_z^3 P(z_*; \zeta_*, \bar{\zeta}_*) / 3! \right]^{1/3} = 0.3175679 + 0.2106751 i.$$

The normalised local imaging polynomial is again

$$P_{\text{loc}}(w; v, \bar{v}) = P(z_* + (t + w_c)/\lambda; \zeta_* + v, \bar{\zeta}_* + \bar{v}) = \mathcal{U}(t; v, \bar{v}) W(t; v, \bar{v}). \quad (72)$$

Form $R_W(m, v, \bar{v}) = \prod_{j=0}^3 W(\omega^j m^{1/3}, v, \bar{v})$ and observe that $R_W = (-2.66759 \cdot 10^{-7} - 3.9926 \cdot 10^{-6} i)m^2 + (1.14296 + 0.331717 i)m^3$, so both constant and linear terms in m are missing. This is the case of accidental multiplicity. For the centred, monic depressed cubic $W(t) = t^3 + pt + q$ at a cusp ($[t^2]W \equiv 0$), the $d = 3$ cyclotomic product over the geode lifts $t = \omega^j m^{1/3}$ has the closed form

$$R_W(m; v, \bar{v}) = \prod_{j=0}^2 W(\omega^j m^{1/3}) = (m + q)^3 + p^3 m = q^3 + (3q^2 + p^3)m + 3q m^2 + m^3.$$

Thus at parameter values where the combinations $q \approx 0$ and $3q^2 + p^3 \approx 0$ (numerically) hold, the constant and m^1 terms are suppressed and one observes $R_W(m; v, \bar{v}) \approx a m^2 + b m^3$ (up to the nonvanishing unit from the Weierstrass factorisation). This signals an *accidental extra multiplicity* in m at that epoch. Consistently with Section 3, we first form the square-free scalar $\tilde{R}_W = R_W / \text{gcd}_m(R_W, \partial_m R_W)$ and only then set $A = \partial_m \tilde{R}_W(0)$, $B = -\tilde{R}_W(0)$, and the prepared source $U = B/A$. In practice, dividing out the common m -factor (often m or m^2 at such points) restores a linear-in- m scalar and a well-conditioned U . Dividing out m^2 yields a linear-in- m scalar; solving it at this epoch gives $m = 1.15032 \times 10^{-6} + 3.15936 \times 10^{-6} i$. We proceed with the root lifting using the anisotropic seeds of equation (36). We get $t_k = (0.00792713 + 0.00110449 i, -0.0132836 + 0.0164089 i, 0.0053565 - 0.0175134 i)$ and after five steps of Newton polish get the physical roots to the machine precision: $z_{1,2,3} = (0.8531663 + 0.5126516 i, 0.84633898 + 0.5607243 i, 0.8440857 + 0.4603394 i)$.

Preparation–invariant kernel $\varphi(m)$.—From the centred pure- m jet of the square-free scalar,

$$\tilde{R}(m; 0, 0) = r_3 m^3 \left(1 + \delta_1 m + \delta_2 m^2 + \delta_3 m^3 + \delta_4 m^4 + \dots \right),$$

we absorb r_3 and define the preparation–invariant kernel

$$\varphi(m) = \frac{1}{1 + \delta_1 m + \delta_2 m^2 + \delta_3 m^3 + \dots} = \left(1 - \sum_{r \geq 1} \alpha_r m^r \right)^{-1},$$

with $\alpha_r = -\delta_r$. For this triple-lens cusp the first kernel coefficients are

$$\alpha_1 = -(249.579 + 360.576 i), \quad \alpha_2 = 135853. + 102306 i, \quad \alpha_3 = -(1.63242 \cdot 10^7 + 9.44856 \cdot 10^6 i),$$

with higher $\alpha_{r \leq 10}$ nonzero as well. In the HC language of Section 9 this example has signature $\text{Sig}_R = (3; \alpha_1, \alpha_2, \alpha_3, \alpha_4, \dots, \alpha_{10})$, which is substantially “stiffer” (larger, more complex coefficients) than in the previous triple lens example, reflecting the strongly distorted local geometry of this lens.

Certified radius and stiffness of the kernel.—Using the majorant kernel $\widehat{\varphi}(m) = (1 - \sum_{r=1}^4 |\alpha_r| m^r)^{-1}$ and the characteristic condition $\sum_{r=1}^4 (r+1) a_r m^r = 1$ with $a_r = |\alpha_r|$, one obtains an indicative seed radius $\widehat{\rho}_U \approx 2.5 \times 10^{-2}$ for the HC series $m(U)$. For the tangential track considered here we continue slightly beyond this value (to $u \simeq 0.033$, corresponding to $|U| \sim 0.03$) and observe that the geode+Newton reconstruction remains accurate and stable, suggesting that the majorant-based $\widehat{\rho}_U$ is conservative. The large, complex coefficients α_r thus manifest as a “stiff” kernel with a relatively small guaranteed radius, but the practical convergence extends somewhat further.

Geometric interpretation: near-tangential cusp crossing.—The second triple-lens configuration considered here is geometrically exceptional: the source trajectory, launched from the cusp point ζ_* along the real axis, proceeds almost exactly along the caustic’s tangent. The local caustic branch at this cusp is inclined by barely 0.6° to the real axis, so as the source advances along the real axis it does not pierce the caustic frontally but slides along it: a near-glancing encounter that keeps the source inside the cusp envelope over an extended interval of $\text{Re}(\zeta)$. A displacement of order 10^{-4} in $\text{Re}(\zeta)$ is sufficient to toggle the system between four and six physical images, while a merging pair coalesces on the critical curve before separating again.

Figure 3(c) displays the three image trajectories in the complex image plane as the source moves along this near-tangential track. One of the branches (shown in green) exhibits a sharp apparent “jump” across the critical curve. This feature is not a numerical artefact: a small change in $\text{Re}(\zeta)$ forces the associated root to switch sheets on the Riemann surface of the imaging polynomial, so its projection in the $(\text{Re}(z), \text{Im}(z))$ -plane appears to jump, even though in the geode variable m the continuation remains perfectly analytic. In the m -representation the analytic branch passes smoothly through the fold where the images coalesce, and the HC series of $m(U)$ remains valid throughout. The discontinuity visible in the plot is therefore imposed purely by the near-tangential geometry, while the underlying geode expansion remains continuous and well-behaved.

This triple-lens cusp examples show that the geode/HC construction applies unchanged to fully physical, non-holomorphic lens mappings and remains robust even in geometrically extreme situations. The preparation-invariant kernel $\varphi(m) = (1 - \sum_{r \geq 1} \alpha_r m^r)^{-1}$ has large, complex coefficients, leading to a relatively small certified seed radius $\widehat{\rho}_U$, yet the HC seeds plus Newton on decic P recover all three image branches with machine-precision residuals along a quasi-tangential source track. In the geode variable the continuation across the fold is smooth and single-valued; the apparent “jump” in Figure 3(c) is entirely due to the projection of the Riemann surface onto the $(\text{Re}(z), \text{Im}(z))$ -plane. Together with Examples 4–6, this underscores the central novelty of the method: a single, preparation-invariant analytic branch suffices to track all local microlensing images across folds and cusps, regardless of global degree, kernel complexity, or lens geometry.

8. CONSEQUENCES: MAGNIFICATIONS, FINITE-SOURCE KERNELS, AND ASTROMETRIC CENTROIDS

In this section we specialize the geode preparation of Section 3 to a fold ($d = 2$) and record the resulting preparation-invariant laws for point- and finite-source observables. All inputs are local jets at the multiple image; no global solution of the lens polynomial is required. This recovers the standard fold scalings and finite-source kernels of B. S. Gaudi & A. Petters (2002a,b); M. D. Albrow et al. (2001) in a form where all lens dependence is compressed into a small set of jet-derived invariants with certified error control. A consolidated comparison of HC signature and spectrum across our worked examples is deferred to Section 9.

(i) *Fold normal form and geode.*—After centring and normalising (Section 3), the local imaging polynomial factors as

$$P_{\text{loc}}(w_c + t; v) = \mathcal{U}(t, v) W(t, v), \quad W(t, v) = t^2 + p_0(v), \quad \mathcal{U}(0, 0) \neq 0,$$

where $v = \zeta - \zeta_*$ and $t = w - w_c(v)$, with $w_c(0) = 0$ and $p_0(0) = 0$. Introducing the fold geode $m = t^2$, the square-free scalar is given by (21) so the image-side kernel is trivial, $\varphi \equiv 1$, and $m = -p_0(v)$ to all orders. In particular, the Lagrange variable U coincides with m , and the HC series collapses to $m(U) = U$ exactly.

Let τ be the signed normal offset in the source plane (positive on the two-image side), and write

$$p_0(v) = -\alpha_0 \tau + O(\tau^2), \quad \alpha_0 > 0,$$

where α_0 is a preparation-invariant function of the local jets (captured explicitly in Section 3). Define the fold scales

$$u_f = \alpha_0, \quad \alpha = u_f^{-1/2}.$$

The two local branches in the centred image coordinate are then

$$t_{\pm}(\tau) = \pm\sqrt{m} = \pm\sqrt{\alpha_0\tau} + O(\tau) = \pm\frac{\sqrt{\tau}}{\alpha} + O(\tau),$$

realising the canonical $t \sim \pm\tau^{1/2}$ fold behaviour.

(ii) *Point-source pair: magnification and centroid.*—Let $\mu_{\pm}(\tau)$ be the signed magnifications of the two fold images, and set

$$\mu_{\text{pair}}(\tau) = \mu_{+}(\tau) + \mu_{-}(\tau), \quad \Theta_{\text{pair}}(\tau) = \frac{\mu_{+}z_{+} + \mu_{-}z_{-}}{\mu_{\text{pair}}(\tau)}.$$

If $\hat{\mathbf{n}}$ is the unit normal to the critical curve at the base image, a standard jet calculation (invariant under admissible coordinate changes) gives

$$\mu_{\text{pair}}(\tau) = \frac{\sqrt{u_f}}{\sqrt{\tau}} \left(1 + O(\tau^{1/2}) \right) = \frac{1}{\alpha\sqrt{\tau}} \left(1 + O(\tau^{1/2}) \right),$$

$$\Theta_{\text{pair}}(\tau) - z_c(0) = B_f \tau^{1/2} \hat{\mathbf{n}} + O(\tau), \quad B_f > 0,$$

where u_f and B_f are preparation-invariant functions of the local jets. Thus the usual $1/\sqrt{\tau}$ magnification and $\tau^{1/2}$ centroid approach near a fold follow directly from the geode normal form with no global solve, and all lens dependence is encoded in the scalars (u_f, B_f) . In the limit of vanishing source size these expressions coincide with the classical fold asymptotics derived in [B. S. Gaudi & A. Petters \(2002b,a\)](#).

(iii) *Finite-source photometry and astrometry.*—For a circular source of angular radius ρ_* centred at signed distance τ , define the dimensionless offset

$$s = \frac{\alpha\tau}{\rho_*} = \frac{\tau}{\rho_*\sqrt{u_f}}.$$

With linear limb-darkening coefficient Γ the fold-pair magnification takes the universal 1D kernel form

$$\mu_{\text{pair}}^{\text{fs}}(\tau; \rho_*) = \rho_*^{-1/2} \left[(1 - \Gamma) G_0(s) + \Gamma G_{1/2}(s) \right],$$

where G_0 and $G_{1/2}$ are the standard chord-integral kernels and $G_{\nu}(s) \sim s^{-1/2}$ as $s \rightarrow +\infty$, reproducing the point-source law. The flux-weighted centroid projected on $\hat{\mathbf{n}}$ is

$$(\Theta_{\text{pair}}^{\text{fs}}(\tau; \rho_*) - z_c(0)) \cdot \hat{\mathbf{n}} = \frac{\rho_*^{1/2}}{\alpha} \frac{(1 - \Gamma) K_0(s) + \Gamma K_{1/2}(s)}{(1 - \Gamma) G_0(s) + \Gamma G_{1/2}(s)} B_f, \quad \frac{K_{\nu}(s)}{G_{\nu}(s)} \sim s^{1/2} \text{ as } s \rightarrow +\infty, \quad (73)$$

These expressions reproduce the fold-crossing kernels used in [B. S. Gaudi & A. Petters \(2002a,b\)](#); [M. D. Albrow et al. \(2001\)](#), but now with explicit identification of u_f and B_f as preparation-invariant jet combinations and with a built-in truncation-error control from the geode construction.

(iv) *Analyticity and truncation control.*—For a fold the Lagrange equation is $m = U$ *globally*, so there is no branch point in the U -plane; the HC kernel is trivial and $m(U)$ is entire. Practical truncation is therefore governed solely by the source-side series of $p_0(\zeta)$ and $z_c(\zeta)$. If

$$p_0(\zeta) = \sum_{n \geq 1} c_n (\zeta - \zeta_*)^n$$

is truncated at order N and used on $|\zeta - \zeta_*| \leq r$, Cauchy's estimate gives

$$\left| p_0(\zeta) - \sum_{n=1}^N c_n (\zeta - \zeta_*)^n \right| \leq \frac{M_{p_0}(r)}{r - |\zeta - \zeta_*|} \left(\frac{|\zeta - \zeta_*|}{r} \right)^{N+1}, \quad M_{p_0}(r) = \max_{|\xi - \zeta_*| = r} |p_0(\xi)|.$$

With $m = -p_0$ and $t_{\pm} = \pm\sqrt{m}$, perturbations propagate as

$$|\delta t_{\pm}| \leq \frac{1}{2} |m|^{-1/2} |\delta m| = \frac{1}{2} (\alpha_0 \tau)^{-1/2} |\delta m|,$$

and one Newton update on $W = t^2 + p_0$,

$$t \leftarrow t - \frac{t^2 + p_0(\zeta)}{2t},$$

squares the seed error whenever $t \neq 0$ (or one can use the exact $t = \pm\sqrt{-p_0}$ very near the axis). This provides a simple, fully constructive truncation-error bound for the fold case, with all constants determined by local jets.

(v) *Cusps*.—For cusps ($d = 3$) the same construction applies with $m = t^3$ and a nontrivial preparation-invariant kernel φ (Section 3). The HC series $m(U) = \sum_{n \geq 1} M_n U^n$ then has a finite analyticity radius ρ_U determined by the characteristic system; seeds $t = \omega m^{1/3}$ are polished on the centred cubic W , as implemented in Examples 5 and 7. The fold case provides the simplest instance in which all these ideas can be written in closed form while remaining directly relevant to finite-source photometry and astrometric centroids.

9. CLASSIFICATION BY HYPER-CATALAN SIGNATURE AND SPECTRUM

The universal Lagrange form of Section 3 gives a preparation-invariant description of every local multiple image:

$$m = U \varphi(m), \quad \varphi(0) = 1, \quad U = \Lambda(\zeta, \bar{\zeta}), \quad (74)$$

valid for any analytic lens polynomial and multiplicity $d \geq 2$. This allows the characteristics of optical catastrophes (folds, cusps, higher) to be extended and quantified beyond their Thom–Arnold topological type.

In addition to the classical type (fold A_2 , cusp A_3 , etc.), we introduce two complementary analytic moduli: the Hyper–Catalan (HC) signature, capturing intrinsic kernel coefficients that control sparsity and stiffness of the single-series solution $m(U)$ and the HC spectrum, encoding the certified analyticity radius of $m(U)$ via the location of branch points in the U –plane. Together they quantify how “stiff” or “soft” a local mapping is and how fast its HC expansion converges, features not captured by purely topological classification.

Definition (HC signature).—At the base point, write $\varphi(m) = (1 - \sum_{r \geq 1} \alpha_r m^r)^{-1}$. The tuple $\text{Sig}_R = (d; \alpha_1, \dots, \alpha_R)$ of first nonzero α_r is the HC signature.

Definition (HC spectrum and radius).—Branch points satisfy $\Delta(m) = \varphi(m) - m\varphi'(m) = 0$ with $U = m/\varphi(m)$. The HC spectrum is $\Sigma = \{(m_*, U_*)\}$ and $\rho_U = \min_{(m_*, U_*) \in \Sigma} |U_*|$.

In practice R is small: for the binary-lens cusp (Example 5) only α_1, α_2 are nonzero, whereas the decic with resonant unit (Example 6) has a single nonzero α_7 and the triple-lens cusp (Example 7) exhibits a “stiff” kernel with several large complex α_r . Beyond the Thom–Arnold topological type, observational analyses of microlensing variability demonstrate that subtle, quantitative features of the local caustic geometry carry physical information (R. Gil-Merino et al. 2005). The HC signature isolates these analytic moduli in a preparation-invariant way.

Classification.—For any local multiple image of multiplicity $d \geq 2$:

- (i) Compute $w_c(v, \bar{v})$ and the monic factor $W(t; v, \bar{v})$ from the Weierstrass preparation of P_{loc} .
- (ii) Form the geode $m = t^d$ and the square-free scalar $\tilde{R}(m; v, \bar{v})$ by cyclotomic product and gcd.
- (iii) Extract the kernel $\varphi(m)$ from $\tilde{R}(m; 0, 0)$ and record the HC signature $\text{Sig}_R = (d; \alpha_1, \dots, \alpha_R)$.
- (iv) Solve the characteristic system (31–32) to obtain the HC spectrum Σ and the analyticity radius ρ_U .

This classification separates topological type (fold versus cusp) from analytic moduli (HC signature and spectrum) and yields a unified, preparation-invariant description of all local microlensing caustics.

10. CONCLUSION

This work goes beyond the classical catastrophe description of folds and cusps by introducing and applying, for the first time in lensing, the preparation-invariant Hyper–Catalan (HC) construction. The universal Lagrange form (74) is shown to govern *all* local multiple images (folds, cusps, higher) of analytic lens polynomials, with U capturing source transport and φ capturing image-side geometry. From this single-series framework we obtain quantitative, model-agnostic moduli: the HC signature $(d; \alpha_1, \alpha_2, \dots)$ and the HC spectrum Σ , which provide explicit sparsity structure for the series, certified convergence, and constructive tail bounds. The construction is degree-agnostic and extends seamlessly to non-holomorphic global maps (e.g. the triple lens) once locally Weierstrass-centred.

Decoupling and portability.—The method separates source-side transport $U = \Lambda(v, \bar{v})$ from the image-side kernel $\varphi(m)$, so the same kernel governs different lenses once they are centred, while Λ carries model-specific geometry. This decoupling allows local kernels to be reused across models, with only the source transport recomputed.

Certified reconstruction.—The HC series $m(U) = \sum_{n \geq 1} M_n U^n$ supplies analytic seeds $t = \omega m^{1/d}$ ($\omega^d = 1$) that reach machine precision after a short Newton polish on the centred Weierstrass factor $W(t; v, \bar{v}) = 0$, without solving the global eliminant. Majorant kernels $\hat{\varphi}$ give explicit truncation errors for any $|U| < \rho_U$, providing rigorous control of approximation errors.

Consistency across models.—The same construction (centre \rightarrow monic $W \rightarrow$ geode $m \rightarrow m = U\varphi(m)$) was validated on: (i) an artificial fold (recovering the classical finite-source kernels and centroids with jet-based invariants), (ii) a physical binary-lens cusp, (iii) an artificial decic cusp with a nontrivial resonant kernel, and (iv) physical triple-lens cusps with a non-holomorphic global map. In each case, the HC seeds plus Newton polish reproduce all image branches with high precision inside the certified radius. The resulting analytic derivatives facilitate gradient-based inference, a capability increasingly required in modern microlensing constructions (M. T. Penny et al. 2019b; N. Kains et al. 2009). Such features enable real-time, robust analysis of fold/cusp crossings in surveys like OGLE or Roman.

Strict vs preparation-invariant gauge.—In a strict gauge, point-mass folds/cusps have $\varphi_{\text{strict}} \equiv 1$; in the preparation-invariant convention adopted here, the base-point m -unit is retained in φ , explaining the nontrivial kernels observed in the binary and triple examples. This choice keeps all physically relevant resonances and analytic structure visible in the HC signature.

Analytic derivatives and inference.—Because U , φ , and $m(U)$ are analytic, all parameter derivatives exist and are stable, enabling gradient-based inference with provable convergence control. Derivatives of image positions, magnifications, and centroids with respect to lens parameters follow from termwise differentiation of $m(U)$ and the local lift, rather than from finite-difference approximations on high-degree root solvers.

Scope and outlook.—The framework does not depend on the polynomial degree and accommodates resonant analytic units (shear, ellipticity, multi-plane couplings) via the HC signature. Future work includes higher- d singularities, certified multi-source compositions, and data-driven priors on Λ and $\{\alpha_r\}$ for inference in complex lensing scenarios, especially in the regime of dense, Roman-like bulge monitoring campaigns (M. T. Penny et al. 2019a). Complex multi-year events like Gaia16aye, where a full Keplerian orbit and space parallax are required to fit the light curve (Ł. Wyrzykowski et al. 2020), are natural targets for extensions of the geode formalism to fully dynamic lenses.

HC spectrum and signature of the worked examples.—The examples developed in Sections 4–7 provide explicit instances of the HC classification framework. Example 4 (artificial fold) has signature $\text{Sig}_R = (2; 0)$ and trivial kernel $\varphi \equiv 1$, so the geode $m(U) = U$ is entire and the HC spectrum is empty, as expected for a fold. Example 5 (binary-lens cusp) has $\text{Sig}_R = (3; \alpha_1, \alpha_2)$ with two small nonzero coefficients and a moderate analyticity radius $\rho_U \approx 0.56$, reflecting a relatively “soft” cusp of nearly polynomial shape. Example 6 (decic cusp with resonant unit) is governed by a single nonzero coefficient at order seven, yielding the sparse HC series with $\text{Sig}_R = (3; \alpha_7)$ and a radius $\rho_U = 0.651$, characteristic of a highly symmetric resonant kernel. Finally, Example 7 (triple-lens cusp) exhibits $\text{Sig}_R = (3; \alpha_1, \alpha_2, \alpha_3, \alpha_4)$ for a “soft” kernel variant and a “stiff” kernel $\text{Sig}_R = (3; \alpha_1, \dots, \alpha_{10})$ with large coefficients α_r that grow in magnitude with r and a small certified radius $\rho_U^b \simeq 2.5 \times 10^{-2}$, quantifying the extreme local geometry of the near-tangential cusp crossing. Together these fingerprints illustrate how the HC signature and spectrum provide a unified, preparation-invariant set of analytic moduli for all local microlensing singularities: folds, cusps, resonant units, and highly distorted triple-lens caustics, while retaining practical predictive power for photometric and astrometric observables.

The wider context extends beyond Galactic microlensing. In quasar microlensing and strong-lensing substructure, local fold-cusp patches dominate short-scale behaviour; the same preparation/HC construction provides controllable surrogates for image positions, magnifications, and time delays with certified errors (V. Belokurov et al. 2005, 2003; N. Evans & V. Belokurov 2002; V. Belokurov & N. Evans 2002). For planetary statistics, OGLE’s 20-year census of wide-orbit planets (R. Poleski et al. 2021) illustrates the scale of data sets to which preparation-invariant caustic approaches could be applied. In wave-optics regimes the HC spectrum sets the domain of uniform approximations, while the germ $m(U)$ delivers systematic expansions of parameters entering canonical diffraction integrals. Plasma lensing and scintillation admit the same local jets and therefore the same reduction.

There are natural limitations. The construction is local and its efficacy is bounded by $|U| < \rho_U$; approaching ρ_U one must re-centre or pass to uniform approximations informed by the multiplicity pattern in Σ . When caustics overlap or higher-codimension catastrophes are present, a fresh preparation with the appropriate multiplicity d is required. The

quality of the invariants depends on accurate jet extraction; this is algorithmic but must be implemented with care in models with time dependence, external shear, or multi-plane structure.

Several extensions are immediate. Automatic detection of multiplicity and jet extraction can turn the preparation into a subroutine for inference constructions, returning Sig_R , Σ , ρ_U , and kernel parameters together with certified error bounds. Pre-tabulation of fold kernels, centroid ratios, and HC coefficients can accelerate real-time modelling in high-cadence surveys and astrometric monitoring. On the theory side, invariant formulas for higher HC coefficients and systematic treatment of higher-codimension catastrophes and multi-plane maps follow from the same elimination and Lagrange framework (N. Wildberger & D. Rubine 2025; I. M. Gessel 2016; D. Stanton 1988; K. Weierstrass 1879; E. Artin & A. N. Milgram 1998; S. G. Krantz 2001). In all cases the central mechanism remains the same: reduce to the univariate, preparation-invariant germ $m = U\varphi(m)$, compute its Hyper-Catalan series and spectrum, and lift once to the physical images.

ACKNOWLEDGMENTS

N.G.B. acknowledges the support from the HORIZON EIC Pathfinder Challenges project HEISINGBERG (grant 101114978), the EPSRC UK Multidisciplinary Centre for Neuromorphic Computing (grant UKRI982) and the Weizmann–UK Make Connection grant (grant 142568).

AUTHOR CONTRIBUTIONS

G.B. came up with the initial research concept in the astrophysical context, performed numerical calculations, performed formal analysis and validation with some help from N.G.B. N.G.B. came up with the mathematical framework and supervised the project. Both authors wrote the manuscript.

REFERENCES

Albrow, M. D., An, J., Beaulieu, J.-P., et al. 2001, *The Astrophysical Journal*, 549, 759

Alexandrov, A., & Zhdanov, V. 2011, *Monthly Notices of the Royal Astronomical Society*, 417, 541

An, J. H., & Evans, N. W. 2006, *Monthly Notices of the Royal Astronomical Society*, 369, 317

Artin, E., & Milgram, A. N. 1998, *Galois theory*, Vol. 2 (Courier Corporation)

Asada, H. 2009, *Monthly Notices of the Royal Astronomical Society*, 394, 818

Belokurov, V., & Evans, N. 2002, *Monthly Notices of the Royal Astronomical Society*, 331, 649

Belokurov, V., Evans, N. W., & Du, Y. L. 2003, *Monthly Notices of the Royal Astronomical Society*, 341, 1373

Belokurov, V., An, J., Evans, N., et al. 2005, *Monthly Notices of the Royal Astronomical Society*, 357, 17

Birrer, S., Amara, A., & Refregier, A. 2015, *The Astrophysical Journal*, 813, 102

Blackman, J. W., Beaulieu, J.-P., Cole, A. A., et al. 2020, *The Astrophysical Journal*, 890, 87, doi: [10.3847/1538-4357/ab6a10](https://doi.org/10.3847/1538-4357/ab6a10)

Bozza, V. 2010, *Monthly Notices of the Royal Astronomical Society*, 408, 2188, doi: [10.1111/j.1365-2966.2010.17258.x](https://doi.org/10.1111/j.1365-2966.2010.17258.x)

Bozza, V., Bachelet, E., Bartolić, F., et al. 2018, *Monthly Notices of the Royal Astronomical Society*, 479, 5157, doi: [10.1093/mnras/sty1791](https://doi.org/10.1093/mnras/sty1791)

Chang, K., & Refsdal, S. 1979, *Nature*, 282, 561

Chang, K., & Refsdal, S. 1984, *Astronomy and Astrophysics* (ISSN 0004-6361), vol. 132, no. 1, March 1984, p. 168–178. Sponsorship: Deutsche Forschungsgemeinschaft., 132, 168

Dominik, M. 2004, *Monthly Notices of the Royal Astronomical Society*, 353, 69

Erdl, H., & Schneider, P. 1993, *Astronomy and Astrophysics*, 268, 453

Evans, N., & Belokurov, V. 2002, *The Astrophysical Journal*, 567, L119

Gaudi, B. S., & Petters, A. 2002a, *The Astrophysical Journal*, 574, 970

Gaudi, B. S., & Petters, A. 2002b, *The Astrophysical Journal*, 580, 468

Gessel, I. M. 2016, *Journal of Combinatorial Theory, Series A*, 144, 212, doi: [10.1016/j.jcta.2016.06.008](https://doi.org/10.1016/j.jcta.2016.06.008)

Gil-Merino, R., Wambsganss, J., Goicoechea, L. J., & Lewis, G. F. 2005, *Astronomy & Astrophysics*, 432, 83

Gould, A., & Gaucherel, C. 1997, *The Astrophysical Journal*, 477, 580, doi: [10.1086/303705](https://doi.org/10.1086/303705)

Hu, Z., Zhu, W., Gould, A., et al. 2024, Monthly Notices of the Royal Astronomical Society, 533, 1991, doi: [10.1093/mnras/stae1906](https://doi.org/10.1093/mnras/stae1906)

Kains, N., Cassan, A., Horne, K., et al. 2009, Monthly Notices of the Royal Astronomical Society, 395, 787

Krantz, S. G. 2001, Function Theory of Several Complex Variables, 2nd edn. (American Mathematical Society)

McGill, P., Smith, L. C., Evans, N. W., Belokurov, V., & Lucas, P. W. 2019, Monthly Notices of the Royal Astronomical Society: Letters, 487, L7

Nucita, A. A., De Paolis, F., Ingrosso, G., Giordano, M., & Manni, L. 2016, The Astrophysical Journal, 823, 120, doi: [10.3847/0004-637X/823/2/120](https://doi.org/10.3847/0004-637X/823/2/120)

Penny, M. T., Gaudi, B. S., Kerins, E., et al. 2019a, The Astrophysical Journal Supplement Series, 241, 3, doi: [10.3847/1538-4365/aafb69](https://doi.org/10.3847/1538-4365/aafb69)

Penny, M. T., Gaudi, B. S., Kerins, E., et al. 2019b, The Astrophysical Journal Supplement Series, 241, 3

Petters, A. O., Levine, H., & Wambsganss, J. 2012, Singularity theory and gravitational lensing, Vol. 21 (Springer Science & Business Media)

Poleski, R., & Yee, J. C. 2019, Astronomy and Computing, 26, 35, doi: [10.1016/j.ascom.2018.11.001](https://doi.org/10.1016/j.ascom.2018.11.001)

Poleski, R., Skowron, J., Mróz, P., et al. 2021, arXiv preprint arXiv:2104.02079

Refregier, A. 2003a, Annual Review of Astronomy and Astrophysics, 41, 645

Refregier, A. 2003b, Monthly Notices of the Royal Astronomical Society, 338, 35

Rhie, S. H. 2003, arXiv preprint astro-ph/0305166

Schneider, P., Ehlers, J., & Falco, E. E. 1992, in Gravitational Lenses (Springer), 157–181

Schneider, P., & Weiss, A. 1986, Astronomy and Astrophysics (ISSN 0004-6361), vol. 164, no. 2, Aug. 1986, p. 237-259., 164, 237

Shalyapin, V., Goicoechea, L., Alcalde, D., et al. 2002, The Astrophysical Journal, 579, 127

Stanton, D. 1988, Ramanujan Revisited, Academic Press, Boston, MA, 525

Tsapras, Y., Cassan, A., Ranc, C., et al. 2019, Monthly Notices of the Royal Astronomical Society, 487, 4603, doi: [10.1093/mnras/stz1404](https://doi.org/10.1093/mnras/stz1404)

Weierstrass, K. 1879, in Functionenlehre (Springer), 105–164

Wildberger, N., & Rubine, D. 2025, The American Mathematical Monthly, 132, 383

Witt, H. 1990, Astronomy and Astrophysics (ISSN 0004-6361), vol. 236, no. 2, Sept. 1990, p. 311-322., 236, 311

Witt, H. J., & Mao, S. 1994, The Astrophysical Journal, 430, 505, doi: [10.1086/174421](https://doi.org/10.1086/174421)

Wyrzykowski, L., Mróz, P., Rybicki, K. A., et al. 2020, Astronomy and Astrophysics, 633, A98, doi: [10.1051/0004-6361/201935097](https://doi.org/10.1051/0004-6361/201935097)